



Turbulence–Combustion Interactions in Premixed and Non-premixed Flames Generated by Hot Active Turbulent Jets

AbdoulAhad Validi¹ · Harold Schock¹ · Farhad Jaber¹

Received: 30 July 2019 / Accepted: 13 July 2020 / Published online: 10 August 2020
© Springer Nature B.V. 2020

Abstract

Direct numerical simulations of turbulent jet ignition (TJI)-assisted combustion of lean hydrogen–air mixtures are performed in a three-dimensional planar jet configuration for various thermo-chemical conditions. TJI is a novel ignition enhancement method which facilitates the combustion of lean and ultra-lean fuel–air mixtures by rapidly and continuously exposing them to high temperature combustion products. Fully compressible gas dynamics and species equations are solved with high order finite difference methods. The hydrogen–air reaction is simulated by a detailed chemical kinetics mechanism. Turbulence–combustion interactions in TJI systems are studied here for different conditions using the flame heat release, temperature, species concentrations, and a newly defined progress variable. Important phenomena such as localized flame extinction/re-ignition and simultaneous existence of premixed/non-premixed flames in TJI-assisted combustion are also investigated.

Keywords DNS · TJI · Flame extinction and re-ignition · Mixed premixed-diffusion flames

Abbreviations

| | |
|---------------|--|
| TJI | Turbulent jet ignition |
| DNS | Direct numerical simulation |
| TPJ | Turbulent plane jet |
| u_i | Velocity component in i th direction (m/s) |
| e_t | Total energy (J/kg) |
| Θ_{ij} | Total stress tensor |
| τ_{ij} | Viscous stress tensor |
| q_i | Heat flux vector (kg/s ³) |

✉ AbdoulAhad Validi
validiab@msu.edu

Harold Schock
schock@msu.edu

Farhad Jaber¹
jaberi@msu.edu

¹ Mechanical Engineering Department, Michigan State University, East Lansing, USA

| | |
|-------------------------|--|
| J_i^α | Species diffusion term (m^2/s) |
| S_α | Rate of mass production/destruction per unit volume for species α due to chemical reaction (kg/s) |
| \mathcal{R} | TJI-assisted combustion progress variable |
| W_α | Molecular weight of species α (kg/mol) |
| R^0 | Universal gas constant ($\text{J}/\text{kg K}$) |
| h_α | Enthalpy of species α (J/kg) |
| C_{p_α} | Specific heat of species α ($\text{J}/\text{kg K}$) |
| $\Delta h_{f,\alpha}^0$ | Enthalpy of formation of species α (J/kg) |
| D | Width of turbulent plane jet (m) |
| U_j | Jet velocity (m/s) |
| U_{co} | Coflow velocity (m/s) |
| r_u | Velocity ratio |
| $x, y, \text{ and } z$ | Stream-wise, cross-stream, and span-wise directions |
| τ_0 | Flow-through time (s) |

1 Introduction

Turbulent jet ignition(TJI) systems can be used to initiate and control chemical reactions in ultra-lean fuel–air mixtures by providing sufficient initial energy through high temperature turbulent jets (Jin et al. 2013; Mittal et al. 2010; Madnia et al. 2000). These systems typically involve pre-chambers and passageways to connect them to a main combustion chamber. An ignition device (e.g. a spark plug) is installed in the pre-chamber to ignite the charge and create a high velocity hot product jet exiting out into the main chamber. This jet initiates and maintains the combustion in main chamber. TJI-assisted combustion of premixed mixtures have been studied before by several investigators, focusing on the transition and the viability of the designed configurations (Boivin et al. 2012; Sadanandan et al. 2007; Iglesias et al. 2012; Djebaili et al. 1995; Dorofeev et al. 1996; Phillips 1972). Validi (2016) studied TJI in various combustion systems via direct numerical simulation (DNS) and large-eddy simulation (LES) methods. This included geometrically simple fundamental flow configurations as well as more complex engine-type systems. A fundamental TJI-assisted combustion of a well characterized turbulent planar jet (TPJ) configuration (Gunnar 1965; Gordeyev and Thomas 2000; Pope 1983, 2000; Hinze 1975) (Fig. 1) is composed of hot products of combustion of a stoichiometric hydrogen–air mixture injected into a lean and relatively cooler premixed hydrogen–air coflow mixture. This configuration is designed such that after a sufficiently long time the TPJ–TJI reaches a “stable” condition which allows collection of stationary turbulence/flame statistics and fundamental insights on the complex flame and turbulence structures in TJI-assisted combustion systems. The physical and chemical processes involved in the TJI–TPJ assisted combustion of a well characterized turbulent planar jet (TPJ) configuration is previously explored (Validi and Jaber 2018). Hydrogen is considered as fuel because of its unique characteristics and well established chemical kinetics mechanism (Ju and Niioka 1994; Bezgin et al. 2013; Vagelopoulos et al. 1994). Numerical simulation of hydrogen and capturing its thin flame front is challenging. Understanding TJI-assisted combustion of hydrogen benefits utilizing this concept using hydro carbon fuels (Validi et al. 2018). Here within a systematic study of TJI–TPJ key flow/combustion parameters, the effects of various thermo-chemical

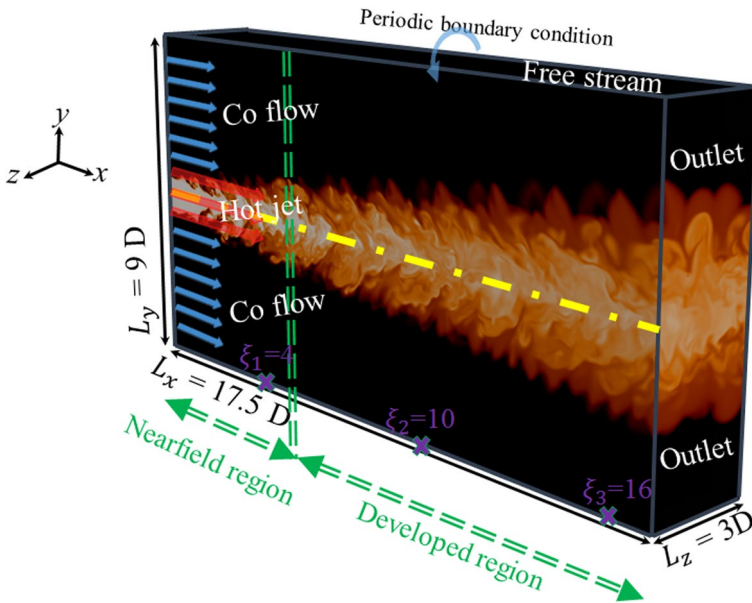


Fig. 1 Schematic of turbulent jet ignition (TJI) in a turbulent plane jet (TPJ) configuration

conditions on the flow-field, combustion zones, and extinction and re-ignition processes are studied. The simulation DNS data are used to investigate the development of premixed/diffusion flame–turbulence interactions. Different coflow compositions are considered, from ultra-lean to moderately-lean mixtures with equivalence ratios of $\phi = 0.1$ to 0.5 . Our results show that TJI is capable of maintaining ultra-lean flames by constantly exposing the mixture to a high temperature jet and decreasing the low flammability limit of premixed mixtures despite the presence of strong localized flame extinctions. The premixed flame propagation, the turbulent jet, and consequently the flame–turbulence interactions are shown to be significantly affected by the coflow mixture composition. There is also a significant change in flame structure when the jet composition is changed from the combustion products of lean to stoichiometric, and then to rich mixtures. Even though the flame is mostly of premixed type in all the simulated conditions, in the case of hot product jet with leftover fuel, simultaneous premixed and diffusion flames are developed, resulting in significant changes in flame structure and an increase in the overall flow temperature.

The complexity and numerical challenges of simulating TJI-assisted combustion arise from the strong coupling of the turbulent flow and thermo-chemical variables over a wide range of temporal and spatial scales, and the highly nonlinear, multicomponent, and unsteady nature of the heat and mass transport and chemical reactions in the hybrid jet-flame setup (James and Jaberri 2000; Pope 2000). The difference of the turbulent scales obtained from scalar fields of spatially evolving reacting and non-reacting jets is investigated by dissipation element analysis in reference Denker et al. (2019). TJI based type of combustion systems often involve a combination of non-premixed to premixed flames which makes their modelling and simulations very difficult (Pope 2000). The flamelet-type combustion models based on G-equation (Peters 1984, 1988) and mixture fraction (Pierce and Moin 2004), each may be used for modelling either premixed or non-premixed flames. Moment closure (Klimenko and Bilger 1999), linear eddy (Kerstein 1992), or

scale-similarity models (Bisetti et al. 2018; Jaber and James 1998) might also be used. Probability density function (pdf) methods (Pope 1985) and Monte Carlo simulation techniques (Jaber et al. 1999) are, however, more attractive for TJI-assisted combustion systems as they can simulate different type of combustion regimes. Flame surface stretching in turbulent jet premixed flames was studied by DNS emphasizing on surface production/destruction rates with respect to Reynolds number (Luca et al. 2019). In this study we use DNS method to avoid modeling uncertainties and to provide a more complete understanding of turbulence and flame structures at all length and time scales.

This chapter is organized as follows. In Sect. 2, the governing equations and numerical methodology are presented. In Sect. 3, the flow configuration is described. In Sect. 4, the effects of the coflow and incoming jet thermo-chemical properties are studied considering various quantities such as temperature, heat release rate, and species concentrations. Section 5 summarizes the main findings and conclusions.

2 Governing Equations and Numerical Methodology

For this DNS study, the following fully compressible, three-dimensional continuity, momentum, energy, and species equations are solved with high order numerical methods.

$$\frac{\partial \rho}{\partial t} + \frac{\partial}{\partial x_i} (\rho u_i) = 0 \quad (i = 1, 2, 3), \quad (1)$$

$$\frac{\partial}{\partial t} (\rho u_i) + \frac{\partial}{\partial x_j} (\rho u_i u_j) = - \frac{\partial p}{\partial x_i} + \frac{\partial \tau_{ij}}{\partial x_j}, \quad (2)$$

$$\begin{aligned} \frac{\partial (\rho e_t)}{\partial t} + \frac{\partial}{\partial x_i} (\rho u_i e_t) = & - \frac{\partial q_i}{\partial x_i} + \frac{\partial}{\partial x_j} (\Theta_{ij} u_i) \\ & + \rho \sum_{\alpha=1}^{N_s} [y_\alpha (u_i + u_{\alpha,i})], \end{aligned} \quad (3)$$

and

$$\frac{\partial}{\partial t} (\rho y_\alpha) + \frac{\partial}{\partial x_i} (\rho u_i y_\alpha) = - \frac{\partial J_i^\alpha}{\partial x_i} + \rho \dot{S}_\alpha. \quad (4)$$

In Eqs. 1–4, the primary variables are the density, ρ , the velocity component in i th direction, u_i , the total energy, e_t , and the scalar mass fraction, y_α , $\alpha \equiv 1, \dots, N_s$ (N_s represents the number of species). Also in these equations, Θ_{ij} is the total stress tensor,

$$\Theta_{ij} = \tau_{ij} - p \delta_{ij}, \quad (5)$$

where viscous stress tensor, τ_{ij} , is obtained by the following Newtonian model:

$$\tau_{ij} = \mu \left(\frac{\partial u_i}{\partial x_j} + \frac{\partial u_j}{\partial x_i} - \frac{2}{3} \frac{\partial u_k}{\partial x_k} \delta_{ij} \right). \quad (6)$$

The heat flux vector, q_i , is given by:

$$q_i = -\lambda \frac{\partial T}{\partial x_i} + \sum_{\alpha=1}^{N_s} (\rho h_{\alpha} y_{\alpha} u_{\alpha,i}), \tag{7}$$

where the first term represents the Fourier heat conduction term and the second term is the heat transport due to “differential diffusion.” The heat transfer due to radiation and Dufour effects has been neglected. The mixture-averaged thermal conductivity, λ , is calculated from the thermal conductivity of individual species. The species diffusion term is evaluated based on the Fick’s law by $J_i^{\alpha} = \rho y_{\alpha} u_{\alpha,i} + \frac{D_{T,\alpha}}{T}$, where $u_{\alpha,i}$, the i th component of diffusion velocity for species α , is calculated by

$$u_{\alpha,i} = \frac{D_{\alpha,N_2}}{y_{\alpha}} \frac{\partial y_{\alpha}}{\partial x_i}. \tag{8}$$

D_{α,N_2} is the binary diffusion coefficient between species α and another species with high concentration (e.g. N_2), however here in a turbulent multicomponent mixture we use effective diffusion coefficient. In order to ensure that the net diffusive flux is equal to zero, $\sum u_{\alpha} y_{\alpha} = 0$ is enforced. The mass flux due to a temperature gradient (Soret diffusion), an important effect in hydrogen combustion, is included and $D_{T,\alpha}$ is the thermal (Soret) diffusion coefficient. In Eqs. 3 and 4, \dot{S}_{α} is the rate of mass production/destruction per unit volume for species α by the chemical reaction. The combustion heat release rate, \dot{Q}_e , is calculated as:

$$\dot{Q}_e = \sum_{\alpha=1}^{N_s} \dot{S}_{\alpha} h_{\alpha}. \tag{9}$$

The total energy and species enthalpy, h_{α} , are expressed as:

$$e_t = \sum_{\alpha=1}^{N_s} h_{\alpha} y_{\alpha} - p/\rho + \frac{1}{2} u_i u_i, \tag{10}$$

and

$$h_{\alpha} = \int_{T_0}^T C_{p_{\alpha}}(T) dT + \Delta h_{f,\alpha}^0, \tag{11}$$

where $C_{p_{\alpha}}$ and $\Delta h_{f,\alpha}^0$ are the specific heat and enthalpy of formation of species α , respectively. The above conservation equations are closed by the equation of state, $p = \rho R^0 T \sum_{\alpha=1}^{N_s} \frac{y_{\alpha}}{W_{\alpha}}$, where W_{α} and R^0 are the molecular weight of species α and the universal gas constant. The Chemkin thermodynamic database (Kee et al. 1989) is used to obtain species thermodynamics and transport properties. The differential diffusion effects (Jaberi et al. 1997) are included in the DNS calculations. The combustion of hydrogen–air is modeled with the detailed chemical kinetics mechanism developed by Stahl and Warnatz (1991). This mechanism, which is extensively used in several previous studies on hydrogen combustion (Ju and Niioka 1994; Vagelopoulos et al. 1994; Arndt et al. 2013; Bezgin et al. 2013), consists of 38 elementary reactions and 9 species (H_2 , O_2 , O , OH , H_2O , H , HO_2 , H_2O_2 , and N_2).

The discretization of the governing equations is based on the compact finite difference scheme (Poinsot and Leleff 1992; Lele 1992), which yields up to sixth order spatial accuracy. In order to avoid numerical instabilities and remove the spurious high frequency fluctuations in the solution, a low pass, high order (up to eighth order), spatial implicit filtering operator is used. The time differencing is based on the third order low storage explicit Runge–Kutta method (Kennedy et al. 2000). The numerical method utilized in this work has been used previously in DNS and LES of low speed and high speed turbulent reacting flows (Banaeizadeh et al. 2013; Afshari et al. 2008; Li et al. 2012; Banaeizadeh et al. 2011; Validi et al. 2018) and is proven to be quite accurate and suitable for the current study.

3 Flow Configuration

The computational configuration considered in this study consists of a spatially developing, three-dimensional turbulent planar jet issuing hot combustion products into a combustible lean premixed ambient coflow. A schematic of the flow configuration, together with the specifications of physical dimensions are presented in Fig. 1. The flow evolves spatially in the stream-wise direction, (x). The free stream boundary conditions are imposed in the cross-stream direction, (y), and periodic boundary conditions are implemented in the span-wise direction, (z). In the simulated TPJ–TJI, the jet expansion is highly affected by the coflow momentum, fuel–air equivalence ratio, and turbulence-controlled flame speed. Therefore, the flow hydrodynamics and geometry have been designed such that a stable and “stationary” combustion is established and time-averaging is made possible.

Table 1 provides the jet and the coflow thermo-chemical properties for different cases, where T_{co} , U_{co} , $Z_{H_{co}}$, and ϕ_{co} represent the temperature, stream-wise velocity, H radical elemental mass fraction, and equivalence ratio of the coflow. The equivalent variables for the incoming jet are denoted by T_j , U_j , Z_{H_j} , and ϕ_{ij} . The variable ϕ_{ij} , however, is the equivalence ratio of an initial hydrogen–air mixture at temperature of 1000 (K) before it burns and gets injected as combustion products with higher temperature at TPJ–TJI inflow. The temperature value of 1000 is selected in order to create a hot product jet with about three times of the coflow temperature (i.e. $T_j \approx 3T_{co}$) and consequently a stable and statistically stationary flame within the selected computational domain. The inlet temperature profile normalized by T_{co} is shown in Fig. 2, which is similar to the velocity profile and smoothly varies from 1 in the coflow to almost 3 in the jet center based on a tangent hyperbolic function. The product species mass fraction values for the simulated cases are provided in Table 2. In Case1 to Case4, the coflow premixed mixture compositions vary from ultra-lean to moderately-lean (i.e. $\phi_{co} = 0.1, 0.2, 0.35,$ and 0.5) with the same coflow temperature and velocity of $T_{co} = 850$ (K) and $U_{co} = 150$ (m/s). In these cases, the same hot product jet with $\phi_{ij} = 1.0$ and $T_j = 2556.0$ (K) is injected so that the coflow composition effects on the turbulence–combustion interactions can be studied independent of the jet condition. Different flames are shown to be developed by changing the coflow equivalence ratio from fast burning to those with significant finite-chemistry effects. The effects of jet composition (lean and rich initial mixtures with $\phi_{ij} = 0.5$ and 2.0) are investigated by considering Case5, Case6, and Case7. Note that by changing the initial jet mixture equivalence ratio from 0.5 to 2.0, the fuel (hydrogen) concentration in the products is changed from $1.9e-7$ to $2.7e-2$ and also the jet temperature is changed from $T_j = 2050$ to 2350 (K). In these cases, the same coflow conditions as those in Case3 are considered. In Case7, the coflow equivalence ratio is the same as that in Case1 but the jet composition is similar to that in

Fig. 2 Inlet temperature and velocity profiles normalized by T_{co} and U_{co}

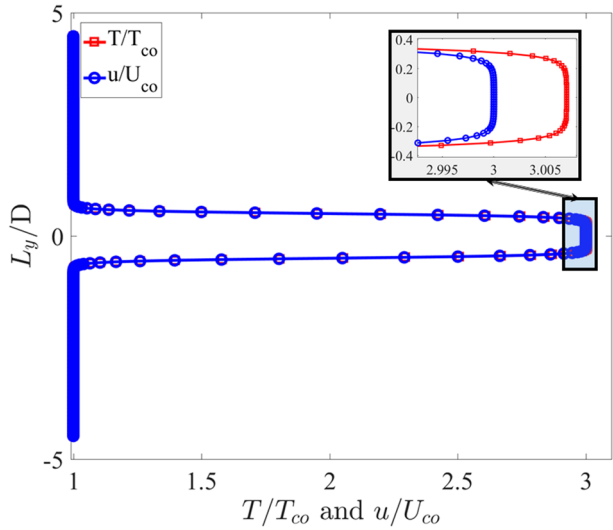


Table 1 Thermo-chemical properties of the incoming jets and coflows for different cases

| Case # | T_j (K) | T_{co} (K) | ϕ_{ij} | ϕ_{co} | Z_{H_j} | $Z_{H_{co}}$ |
|--------|-----------|--------------|-------------|-------------|-----------|--------------|
| Case1 | 2556 | 850 | 1.0e0 | 1.0e-1 | 2.85e-2 | 4.03e-2 |
| Case2 | 2556 | 850 | 1.0e0 | 2.0e-1 | 2.85e-2 | 7.74e-2 |
| Case3 | 2556 | 850 | 1.0e0 | 3.5e-1 | 2.85e-2 | 1.28e-1 |
| Case4 | 2556 | 850 | 1.0e0 | 5.0e-1 | 2.85e-2 | 1.73e-1 |
| Case5 | 2050 | 850 | 5.0e-1 | 3.5e-1 | 1.44e-2 | 1.28e-1 |
| Case6 | 2350 | 850 | 2.0e0 | 3.5e-1 | 5.54e-2 | 1.28e-1 |
| Case7 | 2350 | 850 | 2.0e0 | 1.0e-1 | 5.54e-2 | 4.03e-2 |

Table 2 The species mass fractions in the incoming jets

| Case # | y_{H_2} | y_H | y_{O_2} | y_O | y_{OH} | y_{H_2O} | y_{HO_2} | $y_{H_2O_2}$ | y_{N_2} |
|------------|-----------|--------|-----------|--------|----------|------------|------------|--------------|-----------|
| Case 1–4 | 2.0e-7 | 2.1e-4 | 1.2e-2 | 1.2e-3 | 9.9e-3 | 2.2e-1 | 2.1e-4 | 3.4e-7 | 7.57e-1 |
| Case 5 | 1.9e-7 | 1.3e-6 | 1.1e-1 | 1.7e-4 | 1.8e-3 | 1.2e-1 | 1.6e-6 | 1.7e-7 | 7.55e-1 |
| Case 6 & 7 | 2.7e-2 | 3.3e-4 | 1.2e-5 | 1.5e-5 | 9.9e-4 | 2.4e-1 | 6.7e-9 | 6.8e-9 | 7.24e-1 |

Case6. This case is considered to study the effects of the extra fuel in jet on the diffusion and premixed flames in the ultra-lean coflow mixtures. In all cases considered in this paper, the pressure is atmospheric and the jet velocity is set to be three times of the coflow velocity, $U_j = 3U_{co} = 450$ (m/s). The jet and coflow Mach numbers are equal to 0.43 and 0.245, respectively. The inlet axial velocity profile normalized by U_{co} and is similar to the temperature profile. To produce a well developed turbulent inflow, turbulent fluctuations obtained from an isotropic turbulence field are added to the incoming hot product jet. This field is generated by solving the governing equations with periodic boundary conditions and an initially random, solenoidal, and Gaussian velocity field for a long time (Yaldizli et al.

2008). The intensity of the added turbulence to the hot jet shear layers is chosen to be about 10% of the mean jet velocity. This amount of initial turbulence excites the incoming jet in a short stream wise distance from the jet inlet. To calculate the statistics, the simulations are advanced for three flow-through time, τ_0 , before averaging the variables up to $17\tau_0$. The flow through time, $\tau_0 = 218.75$ (μ s), is calculated based on the average velocity, $U_{ref} = \frac{U_j + U_{co}}{2} = 300$ (m/s), and the stream-wise domain length, $L_x = 17.5 \times D = 65.625 \times 10^{-3}$ (m) ($D = 3.75$ (mm) denotes the incoming jet width). The selected configuration allows the understanding of specific TPJ–TJI physical features that are believed to be invariant of the geometry and common in TJI-assisted combustion systems (Steinberger et al. 1993).

Uniform grid spacing of $\Delta_y = D/60 = 62.5$ (μ m), $\Delta_x = 1.5 \times \Delta_y$, and $\Delta_z = 1.9 \times \Delta_y$, are used in the cross-stream, stream-wise, and span-wise directions. As a detailed chemical kinetics mechanism (Stahl and Warnatz 1991) is incorporated to describe the hydrogen–air combustion, a fine mesh is required for capturing the flame zone and spatial variations of all flame variables (Rehm 1998). The minimum number of grid points covering the flame zone, defined based on H radical and heat release rate profiles, in the entire computational domain is found to be 10. The minimum grid number used for resolving the flame, defined based on the OH radical profile, is more than 15. Examination of other species also confirms that the scalar field is well captured with the adopted grid. To further assess the adequacy of grid resolution for flow variables, we have also computed the local values of the Kolmogorov length scale, $\eta = \left(\frac{\nu^3}{\epsilon}\right)^{1/4}$, and found them to be larger than the grid size. Minimum Kolmogorov length scale values occur close to the inlet at the jet shear layers which is in the order the grid spacing. Further downstream (about $1D$ in axial direction after the inlet) the Kolmogorov length scale increases one order of magnitude which is larger than the maximum grid spacing in the entire domain. The designed computational mesh is believed to be fine enough to accurately resolve all temporal and spatial structures of flow, turbulence, and scalars. The simulations reported in this paper are conducted with the highest resolution involving $800 \times 510 \times 80 \approx 33$ million uniform grid points. The computational time increment is equal to 1×10^{-9} s, which is smaller than the smallest time scales associated with the hydrodynamics and chemistry.

4 Results and Discussion

In this section, the results concerning the effects of coflow and jet conditions on the physio chemical processes involved in the TJI-assisted combustion are discussed. Figure 3a–f present the instantaneous temperature contours at the mid span-wise plane of the three-dimensional computational domain and time $t = 17\tau_0$ for the six simulated cases with conditions provided in Table 1. In the nearfield region, $\xi = x/D \lesssim 4$ shown in Fig. 1, the hot incoming jet causes significant auto ignition at the jet shear layer and surrounding areas, where the jet heats the premixed coflow and ultimately sustains the flame even in the ultra-lean fuel–air mixtures. The amount and location of heat release rate also indicate the auto ignition occurrence in the nearfield region (shown in Figs. 11 and 12). The flame–turbulence interactions, mixing, and reaction of the incoming hot jet with the cooler premixed coflow in the developing shear layer create relatively thick and geometrically complex flames in the nearfield region. Independent of the coflow compositions, similar flame/flow structures are developed in the nearfield region in all cases,

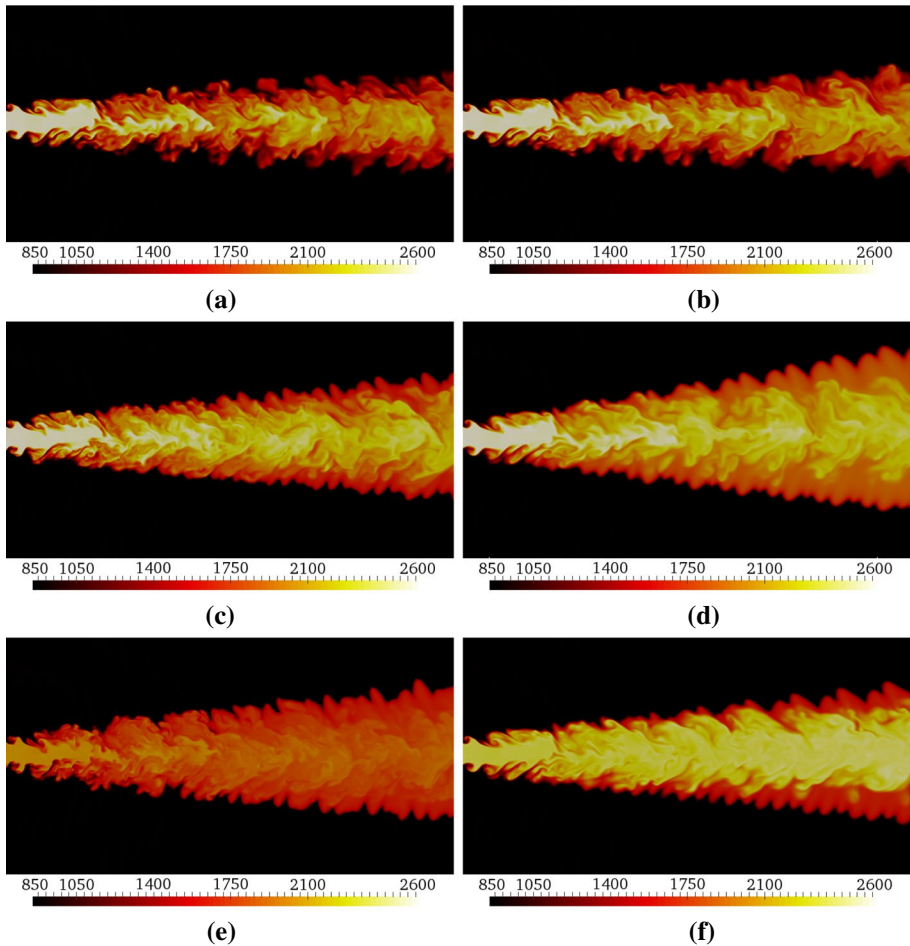


Fig. 3 Instantaneous temperature contours at the mid span-wise plane ($z = 1.5D$) and time $t = 17\tau_0$ for **a** Case1 with $\phi_{co} = 0.1$ and $\phi_{ij} = 1$, **b** Case2 with $\phi_{co} = 0.2$ and $\phi_{ij} = 1$, **c** Case3 with $\phi_{co} = 0.35$ and $\phi_{ij} = 1$, **d** Case4 with $\phi_{co} = 0.5$ and $\phi_{ij} = 1$, **e** Case5 with $\phi_{co} = 0.35$ and $\phi_{ij} = 0.5$, and **f** Case6 with $\phi_{co} = 0.35$ and $\phi_{ij} = 2$

indicating the dominance of the incoming jet effects. In this region, highly distorted turbulent structures are also developed, which strongly interact with the combustion. For Case3, Case5, and Case6 with different jet temperatures and compositions but the same coflow conditions, temperature contours in Fig. 3c, e, f confirm that the nearfield flame/flow structures are indeed influenced more by the incoming jet than the coflow combustion.

In the developed region ($\xi \geq 4$), where the spatially continuous and distorted flame zones exist, the effects of coflow equivalence ratio become more important. In this region, the turbulent premixed flame often gets separated from the incoming jet and core turbulent flow as it propagates into the coflow in the cross-stream direction. This separation develops various distinguishable flow/combustion zones in the simulated TPJ–TJI configurations which can be named as:

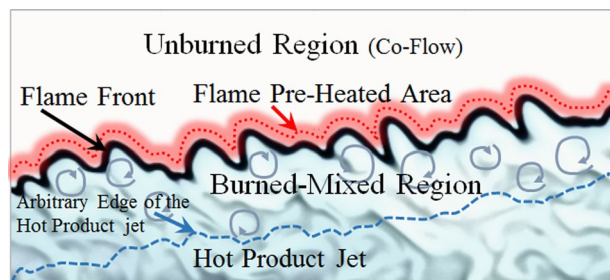
- (1) hot product jet zone,
- (2) premixed flame zone, and
- (3) burned-mixed zone.

Figure 4 shows the schematic of the flow and four main regions in the simulated TJI–TPJ. In order to identify different regions in the flow–flame, we primarily used the temperature and H radical mass fraction, y_H , even though other quantities such as OH mass fraction, vorticity and Baroclinic torque may also be used. It is worthwhile to mention that the details of flow–flame structures may vary by changing thermo-chemical and flow hydrodynamics conditions. However, the general description of various regions identified in TJI–TPJ are still valid.

The hot product jet zone is identified by the highest temperature values close to the jet temperature. The flame zone is identified by relatively low temperature values which are slightly higher than the adiabatic flame temperature of the lean hydrogen–air mixture with the same composition as coflow. The burned-mixed zone is recognized based on the intermediate temperature values, which has some similarities with the burned zone appearing in standard turbulent premixed flames (Pope 1987; Rutland and Trouvé 1993; Clavin 1985), but with a relatively higher temperature and different product species mass fraction values. The complexity of the burned-mixed zone arises from the strong interactions of the inner hot product jet turbulence and composition fields with the lean premixed turbulent flame. Therefore, there may not be well defined boundaries between this zone and its neighboring zones particularly with the hot product jet zone. In the span-wise direction, the flow field is initially homogeneous and isotropic due to the imposed turbulent inflow. It stays homogeneous further downstream, but with considerably larger turbulent scales.

Figure 3 shows that in the developed region ($\xi \geq 4$) the flame expansion and the growth rate of the jet “thermal width” are highly dependent on the coflow mixture conditions. The weak reaction of ultra-lean mixtures in Case1 and Case2 with equivalence ratios of 0.1 and 0.2 (Fig. 3a, b) hardly establishes stable and distinguishable combustion zones, suggesting significant localized flame extinction and re-ignition (more details are provided in Sect. 4.2). However, for Case3 and Case4, with coflow equivalence ratios of 0.35 and 0.5, the flame is stable and widely spreads in the cross-stream directions, leading to separation of flame from the core jet turbulence (Fig. 3c, d). Despite different jet thermo-chemical conditions, the growth and structure of combustion zones for Case5 and Case6 (Fig. 3e, f) are almost the same as those for Case3 (Fig. 3c), suggesting that the initial energy provided by the incoming hot product jet is sufficient to initiate a stable combustion in coflow mixtures with equivalence ratio of 0.35. These results confirm that the combustion in the developed region is very sensitive to the coflow composition, but is less influenced by the incoming jet composition particularly at sufficiently high equivalence ratios. The lower jet

Fig. 4 Various regions in the simulated turbulent planar jet with turbulent jet ignition

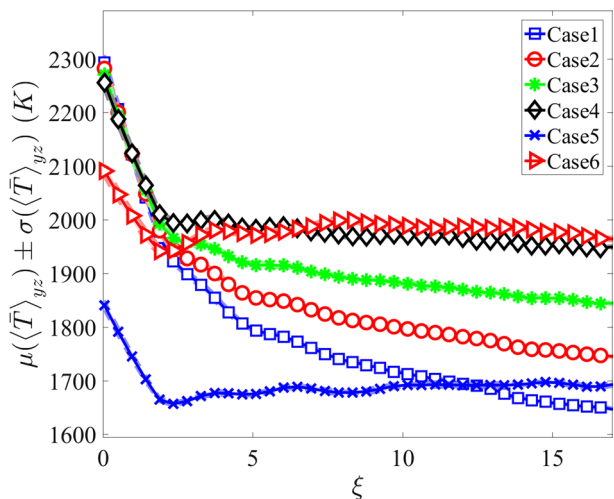


temperature in Case5 (Fig. 3e), slightly affects the flame growth. The unburned hot fuel in the injected jet in Case6 (Fig. 3f) mixes with the available oxidizer in the coflow and establishes stable diffusion flames within the main jet surrounded by the premixed flames. However, the heat release by the diffusion flames has a little effect on the overall jet behavior and the surrounding premixed flame in Case6.

The overall effects of the coflow and incoming jet parameters are further examined in Fig. 5, where the mean and confidence intervals of time and $y - z$ plane averaged temperature, $\mu(\langle \bar{T} \rangle_{yz}) \pm \sigma(\langle \bar{T} \rangle_{yz})$, are plotted at different stream-wise locations for six cases. The time-averaged statistics are calculated from the data gathered for $17\tau_0$. In these calculations, the coflow data are excluded, but the preheated zones of the premixed flame are included, which potentially lower the reported mean temperatures. Evidently, the results associated with the nearfield region are very similar in Case1 to Case4, which show the importance and dominance of the incoming jet properties and turbulent mixing of the hot jet with the coflow. In fact, we found that the time and span-wise averaged profiles of the temperature versus the cross-stream direction at different stream-wise locations (not shown here) are nearly identical in cases with similar incoming jet thermo chemical conditions (Case1–4). In the nearfield region, the maximum temperature, located at the jet centerline, is lower in Case5 and Case6 with lean and rich product jet mixtures. The temperature profiles in the shear layer seem to be dependent more on the coflow composition than the incoming jet composition.

The transition from the nearfield region to the developed region approximately starts at $\xi \approx 3$. In the developed region, the averaged temperature values continuously decrease along the stream-wise direction but with a much higher rate in Case1 in comparison to Case4. This is expected and is due to weaker and lower temperature combustion in the cases with low coflow equivalence ratios. Case5 with a lean initial jet mixture, $\phi_{ij} = 0.5$, exhibits rather different trend in comparison with other cases. For this case, the averaged temperature is initially lower compared to other cases and further decreases in the nearfield region before increasing again in the developed region and reaching to a plateau at downstream locations. A comparison between Case5 and Case3 indicates that even though the flow and combustion are similar in the nearfield region, the temperature is generally lower in Case5 since the temperature of the incoming jet is lower. In the

Fig. 5 Mean and confidence intervals of time and $y - z$ plane averaged temperature, $\mu(\langle \bar{T} \rangle_{yz}) \pm \sigma(\langle \bar{T} \rangle_{yz})$, in the combustion zones at different stream-wise locations, ξ , for Case1 (blue square), Case2 (red circle), Case3 (green asterisk), Case4 (black diamond), Case5 (blue times), and Case6 (red right-pointing triangle). (Confidence intervals are very narrow.)



developed region of Case6 with a rich initial jet mixture, ($\phi_j = 2.0$), the averaged temperature profile plateaus after a small increase, which is similar to that for Case5 but is due to different reasons. The incoming jet temperature in Case6 is lower than that in Case3, but unlike Case5, there is a stable diffusion flame with higher averaged temperature in this case. The presence of non-premixed flame in Case6 is evident in Fig. 3f, where the temperature inside the combustion zones is shown to be considerably higher than those in other cases. The diffusion flame evidently increases the averaged temperature even higher than that in Case3, despite the same coflow conditions.

It has been suggested in reference Valdi (2016) that the approximate location of the flame or the jet thermal half width, D_{half} , in $\overline{TPJ-TJI}$ can be obtained from the peak temperature root mean square (rms), $T_{rms} = (\overline{T^2} - \overline{T}^2)^{1/2}$, since high temperature variations usually occur at the flame zone. Figure 6i shows the temperature rms contours at the mid plane for Case3, representing “high value T_{rms} zones” in the nearfield region, an indication of approximate location of relatively thick premixed/diffusion flames in this region. These high T_{rms} zones also occur in the periphery of the jet at the lean premixed flame zone and the developed region. The jet thermal half width (D_{half}) is measured simply by fitting a straight line (dashed black line shown in Fig. 6i) to the locally maximum T_{rms} values. Figure 6 shows the stream-wise variations of the thermal half width jet, normalized by the incoming jet width, D_{half}/D , for different cases. The maximum and minimum D_{half} values correspond to Case4 and Case1 with the highest and the lowest coflow equivalence ratios. Evidently, D_{half} may not be altered significantly by changing the thermo-chemical properties of the incoming jet or by adding extra fuel or oxygen to the jet. Nevertheless, D_{half} for Case6 is slightly greater than that for Case3, which suggests a small effect of the inner jet diffusion combustion on D_{half} . For the conditions that the combustion is strong and premixed flames are moved far away from the incoming jet, D_{half} is unlikely to be affected by the interactions with the main jet turbulence. It can be concluded that D_{half} is mainly controlled by the premixed flame propagation.

Fig. 6 Thermal half jet width, normalized by the incoming jet width (D_{half}/D), versus stream-wise direction (ξ). (i) contours of rms of temperature, T_{rms} , at the mid span-wise plane, ($z = 1.5D$), for Case3

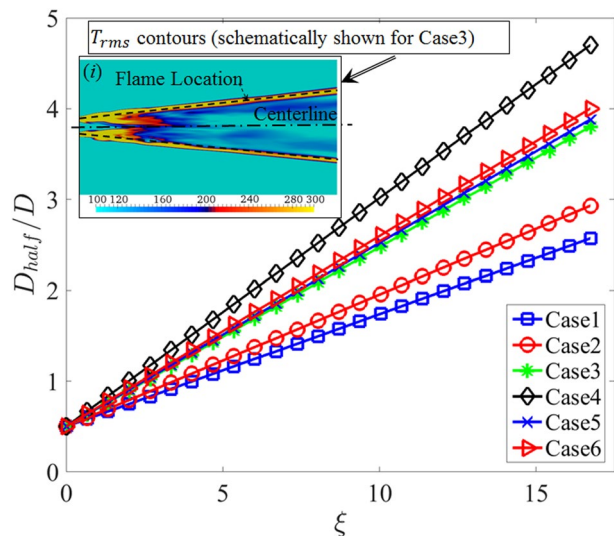


Figure 7a, b show the time and span-wise averaged temperature $\langle \bar{T} \rangle_s$ for non-reacting and reacting cases, respectively. In comparison to the non-reacting case, the jet spreading is considerably more in reacting case. The main cause for this increase in jet span is the turbulent burning velocity. The combustion induced change in flow and turbulence within the burned-mixed and hot product jet zones also has some effects on the jet span. Since these effects can not be well characterized and are expected to be less significant than the flame propagation, they are ignored in developing the following method to calculate turbulent flame speed. Considering points p_N and p_R to be located at the edge of non-reacting and reacting mean jets with the geometrical locations of (x_{p_N}, y_{p_N}) and (x_{p_R}, y_{p_R}) , where $x_{p_N} = x_{p_R}$, one can calculate the jet angles as $\alpha_N = \tan^{-1} \left(\frac{y_{p_N}}{x_{p_N}} \right)$ and $\alpha_R = \tan^{-1} \left(\frac{y_{p_R}}{x_{p_R}} \right)$ by assuming the origin of the angles to be located at the virtual jet origin (Kotsovinos 1976). The turbulent flame speed at any axial location can be calculated as $S_T = \frac{y_{p_R} - y_{p_N}}{t_T}$, where $t_T = \frac{u}{x_{p_N}}$ and u are time and convective velocity. Various analytical, numerical, and experimental studies have reported the hydrogen turbulent flame speed (Lin et al. 2014; Beer et al. 2014; Wang et al. 2015; Seitzman and Lieuwen 2014). Despite differences in thermo-chemical conditions, interestingly the results of our calculations for the hydrogen turbulent flame speed are found to be comparable but slightly higher than those reported in the literature; possibly due to different flow-flame structures in the burned zone.

4.1 Progress Variable for TJI-Assisted Combustion

Our analysis of TJI-assisted combustion in TPJ configuration reveal that a wide range of various premixed to diffusion flames are involved in this type of combustion system. To classify the TJI-assisted combustion regimes and flames under various conditions, a suitable flame variable needs to be defined. The common parameter in analyzing the standard premixed flames is the progress variable, defined by

$$c_{premixed} = \frac{T - T_f}{T_b - T_f}, \tag{12}$$

where T_f and T_b represent the flame and burned zone temperatures. This progress variable conventionally goes to zero and one in the unburned mixture and burned gas zones,

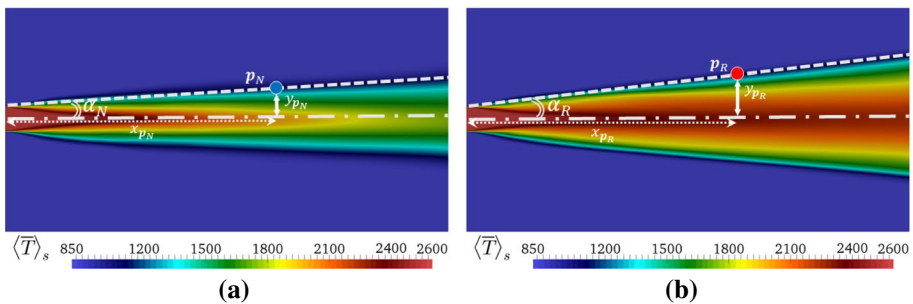


Fig. 7 Contours of time and span-wise averaged temperature and the jet span spread rate for **a** Non-reacting and **b** Reacting cases

respectively. The intermediate values are associated with the flame sheet. However, in the lean burning TJI-assisted systems the maximum temperature is normally associated with the incoming hot jet and not necessarily the burned gases. Therefore, the standard definition (Eq. 12) of the progress variable is not very useful for our analysis; the flowfield information concerning the local, incoming jet, and coflow temperatures must be included.

The challenge of defining a flame variable for TJI-assisted combustion also arises from the coexistence of diffusion and premixed flames. The simultaneous existence of these two types of flames occurs when the incoming product jet contains extra fuel (e.g. Case6 with $\phi_j > 1$). In this condition, the fuel and air streams are getting exposed to each other mostly in the hot product jet zone (the non-premixed flames can occupy a significant part of this zone), which is confined by the premixed flame. One may argue that since the products exist in both fuel and oxidizer streams of the non-premixed regime of the TJI-assisted combustion, a proper alternative definition of the mixture fraction might be based on the elemental conservation equations. But a combination of fuel, oxidizer, or elemental transport equations is derived with the equi-diffusional approximation, which ultimately suppresses the effects of the temperature. Figure 8a shows the mean and confidence intervals of temperature in the combustion zones versus the elemental mixture fraction (based on element H), $f = \frac{z_H - z_{Hj}}{z_{Hco} - z_{Hj}}$, for six cases listed in Table 1. Here, $z_H = \sum_{\alpha=1}^{N_s} \frac{a_H W_H}{W_a} y_\alpha$, $y_{Hco} = \sum_{\alpha=1}^{N_s} \frac{a_H W_H}{W_a} y_{\alpha co}$, and $y_{Hj} = \sum_{\alpha=1}^{N_s} \frac{a_H W_H}{W_a} y_{\alpha j}$ are the local, the coflow, and the incoming jet elemental mass fractions (a_H is the number of element H with molecular weight W_H in the species α with molecular weight W_α). The poor performance of f is evident in this figure as for a fixed f various temperature values are predicted and the effects of jet and coflow cannot be distinguished. Hence, TJI-assisted combustion progress variable not only has to trace the fuel and air streams, but also has to include the temperature effects in a functional form like $\mathcal{R} \approx g(T, T_j, T_{co})h(\phi)$. Here, we define a non-normalized \mathcal{R} as:

$$\mathcal{R} = \left(\frac{T_j - T}{T_j - T_{co}} \right) \phi, \tag{13}$$

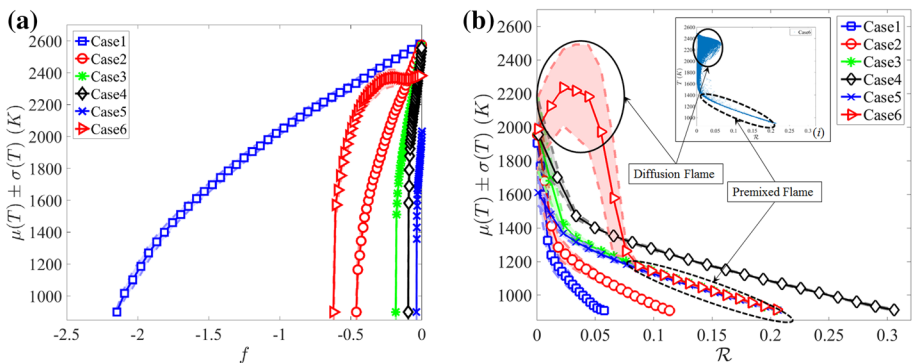


Fig. 8 Mean and confidence intervals of temperature, $\mu(T) \pm \sigma(T)$, in the combustion zone at $t = 17\tau_0$ versus **a** the elemental mixture fraction, f and **b** the TJI combustion progress variable, \mathcal{R} , for Case1 (blue square), Case2 (red circle), Case3 (green asterisk), Case4 (black diamond), Case5 (blue times), and Case6 (red right-pointing triangle). (i) Scatter plot of temperature versus TJI combustion progress variable, \mathcal{R} , for Case6

where T and ϕ , the local temperature and equivalence ratio, are variable. Figure 8b presents the mean and confidence intervals of temperature in the combustion zones versus \mathcal{R} for all 6 cases. The \mathcal{R} values can be related to different combustion zones. For example, $T \rightarrow T_{co}$ and $\mathcal{R} \rightarrow \phi_{co}$ represent the preheated zone in the premixed coflow. The straight line with negative slope shows the transition of the flow from unburned fresh coflow to the burned-mixed zone passing through the premixed flame. At the other side of the flow, $T \rightarrow T_j$ and $\mathcal{R} \rightarrow 0$ represent the hot product jet zone. In the cases with extra fuel in the incoming jet, ϕ_j contribution to \mathcal{R} is more significant, which results in small but greater than zero \mathcal{R} , representing the diffusion flame. The intermediate \mathcal{R} values represent the burned-mixed zone. Further examination of \mathcal{R} in Fig. 8i confirms the ability of this variable to locate the premixed and non-premixed flames in the TPJ–TJI configuration.

In the next section, the effects of coflow equivalence ratio on the TPJ–TJI flow/flame are examined. Changes in the coflow condition significantly affect the flame structure and its interactions with the turbulence. Also, ultra-lean coflow mixtures lead to significant localized flame extinction and re-ignition.

4.2 Flame and Turbulence Structures for Different Coflow Compositions

In the standard flames, OH radical is often used for identifying the flame zone (Lu et al. 2012; Wang et al. 2011; Bezzin et al. 2013). Figures 9a–d show the OH mass fraction contours for Case1 to Case4. Evidently, the OH radicals generated by the lean combustion (very intensively in the nearfield region and less intensively in the developed region) add up to the inflow OH of the incoming product jet, therefore the maximum value of y_{OH} occurs somewhere inside the jet right after the complex thick flame in the nearfield region

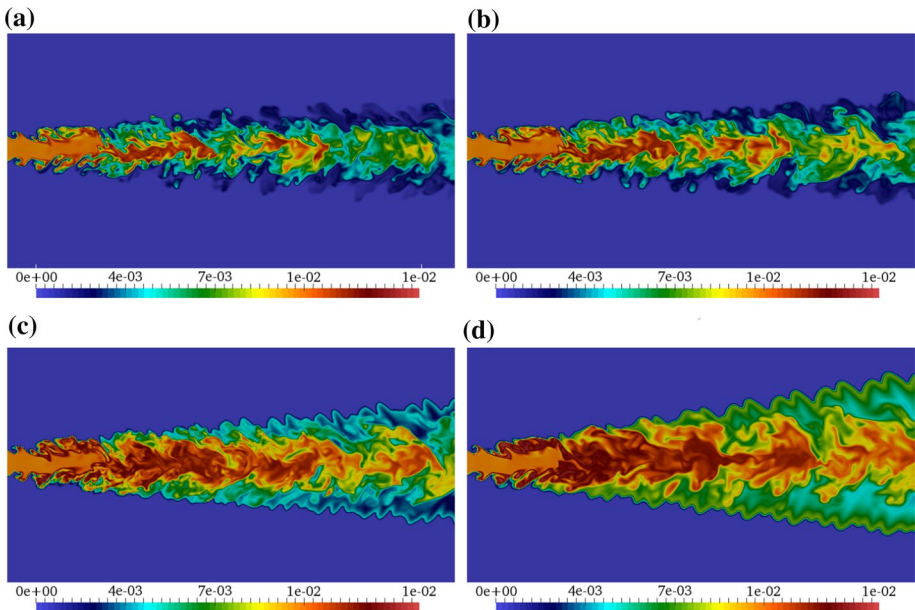


Fig. 9 Instantaneous contours of the OH mass fraction, y_{OH} , at the mid span-wise plane ($z = 1.5D$), and $t = 17\tau_0$ for **a** Case1, **b** Case2, **c** Case3, and **d** Case4

and not at the lean premixed flame front. Due to weak combustion of the ultra-lean coflow mixtures, the OH generation is relatively small and the local maximum values of y_{OH} in the nearfield region are considerably larger than those in the developed region in Case1 and Case2 (Fig. 9a, b). Expectedly, the OH level in Case3 and Case4 increase, on average, due to more stable and stronger premixed combustion. The high y_{OH} values occur further away from the inflow in the stream-wise direction. Figure 9c, d show that y_{OH} values are also locally higher in the flame zone than those in the immediate surroundings. Thus, while OH might be a fair indicator of flame zone when the combustion is sufficiently strong, it cannot locate the flame front or the extent of extinguished flame in ultra-lean mixtures. Other radicals such as H in hydrogen combustion (or CH in hydrocarbon combustion) are potentially more helpful in analysis of TJI-assisted combustion.

Figure 10a–d present the contours of H mass fraction for Case1 to Case4. It can be observed that the maximum value of y_H occurs right at the lean premixed flame front while its values inside the incoming jet, in contrast to y_{OH} , are relatively low. This suggests that the radical H is a better flame marker in the TJI-assisted hydrogen combustion. Note that the color contour maps in Fig. 10 are scaled differently for better capturing of H radical behavior. For all coflow conditions considered in Case1 to Case4, the high values of y_H occur at the edges of the incoming jet in the nearfield region as shear layers develop and generate relatively thick flames. In the developed region of Case4, y_H values are comparable to those in the nearfield region and maximize at the flame front before dropping to very low values in the burned-mixed and hot product zones. Similar trend is observed in Case3, Case2, and Case1 but with smaller local maximum y_H values at the flame front. In Case1 (and to a lesser extent in Case2) the local values of y_H in the flame zone are considerably lower than those in the nearfield and there are some discontinuities in the flame front due to

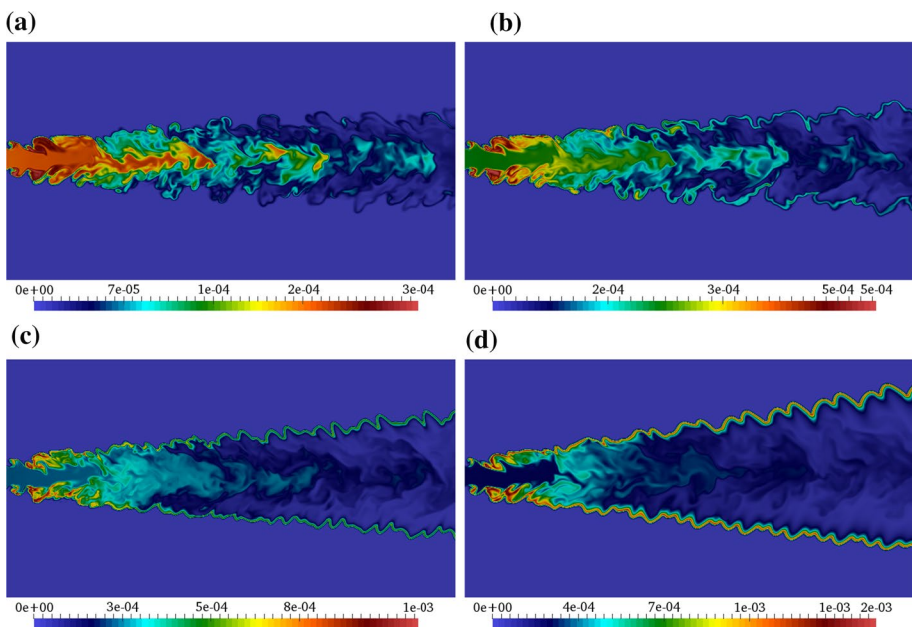


Fig. 10 Instantaneous contours of the H mass fraction, y_H , at the mid span-wise plane ($z = 1.5D$) and $t = 17\tau_0$ for **a** Case1, **b** Case2, **c** Case3, and **d** Case4. (Note that the scale limits are set to the available values in each contour and are not the same.)

localized flame extinction. Our results indicate that H radical mass fraction values are well correlated with the heat of reaction especially in the developed regions.

The combustion heat release rate, \dot{Q}_e , is an important quantity to discern flames and their locations in turbulent reacting flows. The spatial distribution of \dot{Q}_e is highly dependent on the turbulent transport of heat among main core jet, premixed flame, and coflow as well as the chemical reaction. Despite its importance, measuring \dot{Q}_e is challenging (Paul and Najm 1998; Nikolaou and Swaminathan 2014). Here, \dot{Q}_e is obtained from the DNS data via Eq. 9 Najm et al. (1998). Figure 11a–d show the instantaneous contours of heat release rate at the mid span-wise plane for the cases with different coflow equivalence ratios. As explained before, the mixing of the incoming hot jet with cooler premixed coflow in the nearfield region at the reacting shear layer creates relatively thick and geometrically complex flame structure in the TPJ–TJI. The flame structure in the nearfield region might be similar to the corrugated and distributed burning zones in standard premixed flames, where the turbulent eddies are strongly coupled with the thickened and wrinkled flame front. The somewhat distributed and strong reaction virtually vanishes from the main jet as the flow transitions from the nearfield to the developed region and the combustion removes the small scale turbulence. Moving in the stream-wise direction, a spatially continuous, distorted, and concentrated flame is developed in Case4 and Case3 (and to lesser extent in Case2). While the flame propagates in the cross-stream direction into the coflow and moves away from the incoming jet, it becomes thinner and much less affected by the jet turbulence. The \dot{Q}_e contours in Fig. 11b–d clearly show the separation of unburned and burned-mixed zones and the relatively thin distorted premixed turbulent flame in the developed region. Even though the flame and turbulence variables significantly fluctuate in time, they appear to be well stabilized in the developed region particularly in Case2, Case3, and

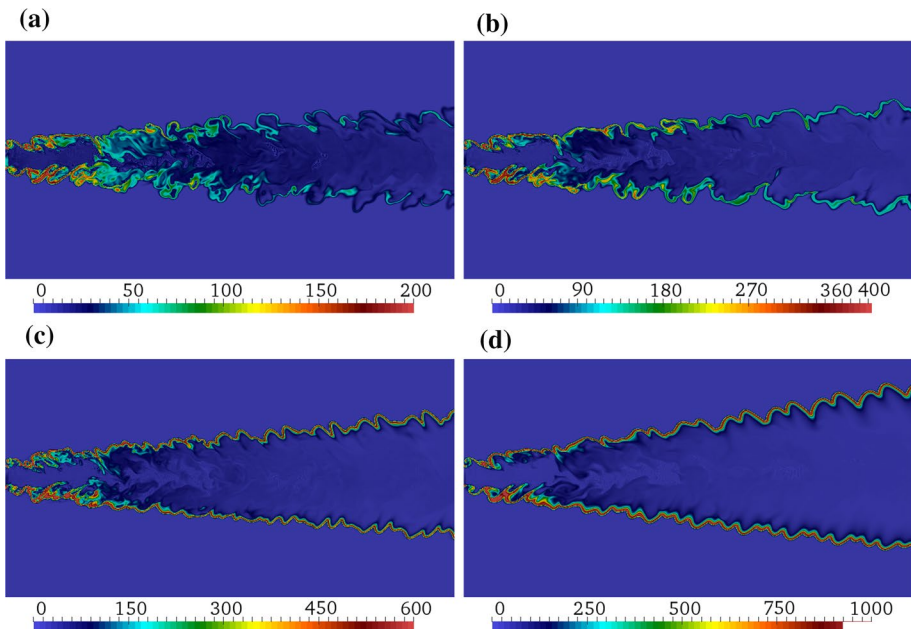


Fig. 11 Instantaneous contours of the heat release rate, \dot{Q}_e (W), at the mid span-wise plane ($z = 1.5D$) and $t = 17\tau_0$ for **a** Case1, **b** Case2, **c** Case3, and **d** Case4. (Note that the scale limits are set to the available values in each case and are not the same.)

Case4. In Case1, the heat release contours (Fig. 11a), consistent with H radical mass fraction contours (Fig. 10a), illustrate relatively high and very low \dot{Q}_e values along the flame front, indicating that the coflow composition in this case is indeed very lean and close to lower flammability limit of hydrogen–air mixtures. The lean flammability limit for hydrogen–air mixture at $T = 359$ (K) is reported to be about 0.14 (Zabetakis 1965). Considering that the coflow temperature in Case1 is higher than the reported value in experimental measurements, the TJI-assisted premixed combustion has a lower lean flammability limit (0.1 in Case1) than the standard premixed combustion, since the fuel–air mixtures are continuously exposed to a high temperature jet.

In Fig. 12, the mean and confidence bounds of the $(y-z)$ plane averaged heat release rates, $\mu(\langle \dot{Q}_e \rangle_{yz}) \pm \sigma(\langle \dot{Q}_e \rangle_{yz})$, are plotted at various stream-wise locations for Case1 to Case4 with different coflow equivalence ratios. The peak combustion heat release values are different in these cases, but occur almost at the same stream-wise location close to the end of the nearfield region. This suggests that the auto ignition becomes more effective where the residence time is sufficiently large, even though the flame is already initiated at the shear layer. This confirms the dominance of the incoming jet hydrodynamics in the nearfield region. In the developed region, a descending heat of combustion with various rates is observed, which indicates different cooling of the jet as it develops. In case1, $\langle \dot{Q}_e \rangle_{yz}$ does not increase so much in the nearfield region and decreases to very small values at the end of the developed region, suggesting a very weak combustion and significant extinction.



The flame stability and extinction are effectively controlled by the interplay of the heat loss from the flame due to turbulent mixing, and the combustion heat release. The heat release is comparatively small in Case1 (and to a lesser extent in Case2), making the TPJ–TJI to operate close to lean flammability limit as shown in Fig. 11a. Figure 13 also shows the contours of \dot{Q}_e for Case1 together with a magnified view of a section of flow/flame field in the developed region. The local extinction and re-ignition events are illustrated by  and , respectively. The spatial and temporal variations in turbulent velocity (particularly at small scales) have significant effects on the flame stretching and folding. With a local increase in stretching effects of turbulence, the gap between the two sides of the flame decreases which leads to local flame extinction and incomplete

Fig. 12 Mean and confidence intervals of $y-z$ plane averaged heat release rate, $\mu(\langle \dot{Q}_e \rangle_{yz}) \pm \sigma(\langle \dot{Q}_e \rangle_{yz})$, at $t = 17\tau_0$ at different stream-wise locations, ξ , for Case1 (blue square), Case2 (red circle), Case3 (green asterisk), Case4 (black diamond)

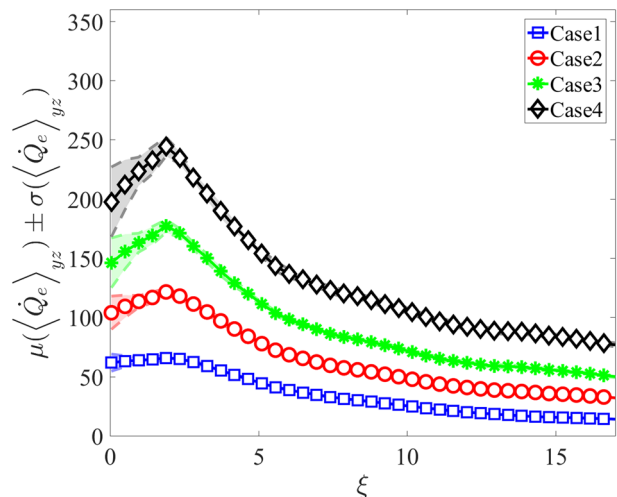
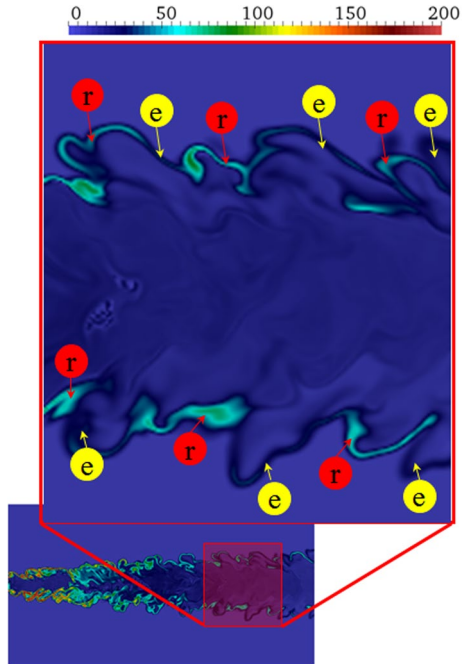


Fig. 13 Localized extinction (e) and re-ignition (r) events around the flame in Case1 with the ultra-lean coflow, identified based on heat release and a magnified view of flow by a factor of 5:1



combustion. As observed in the magnified image, the local flame extinction events are accompanied by a drop in heat release to near-zero values. When the flame front is pushed further away from the hot incoming jet, more local flame extinction events occur. Also, more re-ignition events are observed at locations close to the hot product jet zone, where relatively high heat release values reappear among the extinct flame zones. These confirm that in situations where the premixed flame is close to the hot product jet, the intense interactions and heat transfer from the incoming jet help the flame to continuously re-ignite after extinction. As long as the flame front is connected, lean coflow mixtures stay largely separated from the flame front and hot product inside burned-mixed zone.

Figure 14a–e show the temperature contours (red color) superimposed by the heat release contours (yellow color) for Case1 in area $\xi_2 \leq \xi \leq \xi_3$ at different times. In the right figures, a section of the flame/flow is magnified and tracked in time. In this section, the flame front is initially complex and continuous but starts to break after about $0.17\tau_0$ when the extinction starts and continues to become locally important as shown in Fig. 14b, c. When the flame front gets broken, the combustion induced high-viscosity “dilatation layer” is no longer present to form a barrier keeping high temperature turbulent eddies, hence, they can escape through the holes in the flame front and diffuse into the coflow. The mixing of the diffused hot pockets with the coflow increases the temperature of the preheated zone of the premixed flame at the coflow side which subsequently leads to flame re-ignition (Fig. 14d). The temperature variations between the locally extinguished and re-ignited flames are not very significant, unlike the standard turbulent premixed flames which normally have low flame temperature in regions with significant flame extinction. This is consistent with the results in Fig. This is consistent with the results in Fig. 3a. Figure 14e indeed shows that the extinguished flame is re-ignited by the escaped hot turbulent eddies

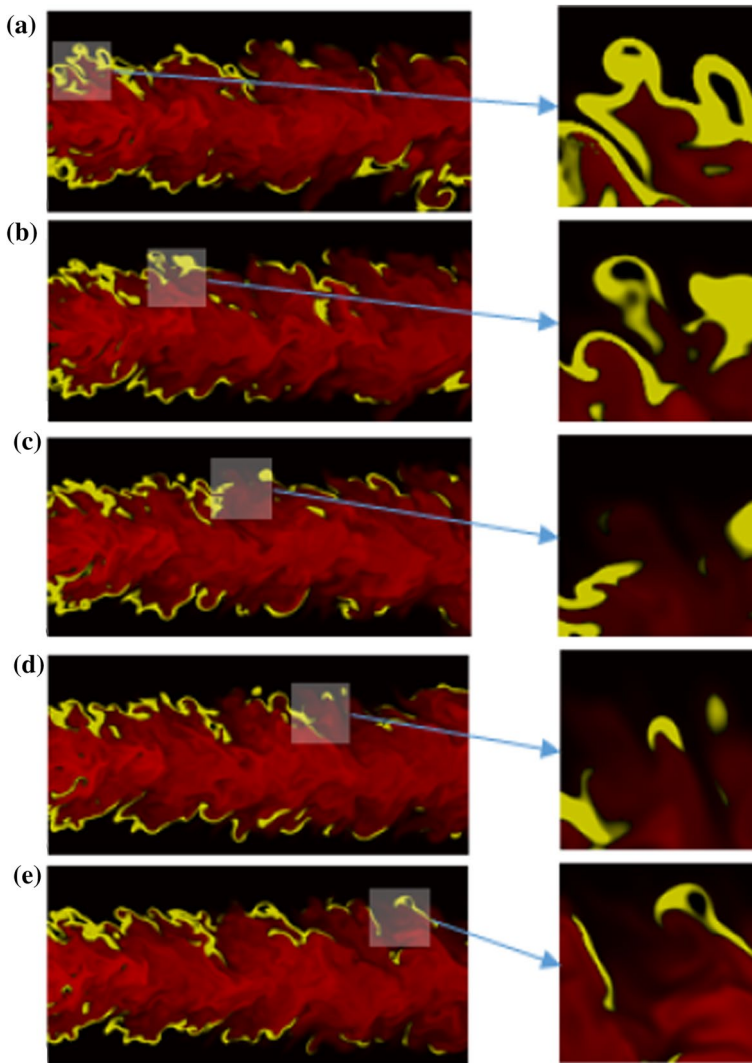


Fig. 14 Instantaneous temperature (red color) contours superimposed by heat release (yellow color) contours in section $\xi_2 \leq \xi \leq \xi_3$ at the mid span-wise plane ($z = 1.5D$) and different times. **a** $t = 17\tau_0$, **b** $t = 17.17\tau_0$, **c** $t = 17.34\tau_0$, **d** $t = 17.52\tau_0$, and **e** $t = 17.69\tau_0$

from downstream locations. Furthermore, the high temperature eddies, which already passed through this section, help to re-ignite the extinguished flames located upstream.

To better understand the compositional flame structure and the local extinction and re-ignition in TPJ–TJI configurations, the scatter plots of \dot{Q}_e versus \mathcal{R} are shown in Fig. 15 for Case1 to Case4. The results for various sections of the flow are included by dividing the flow into three sections: Sec1, (blue square), representing the nearfield region $0 \leq \xi \leq \xi_1$, Sec2, (red diamond), representing the initial part of the developed region $\xi_1 \leq \xi \leq \xi_2$, and Sec3, (black asterisk), representing the end part of the developed region $\xi_2 \leq \xi \leq \xi_3$. The

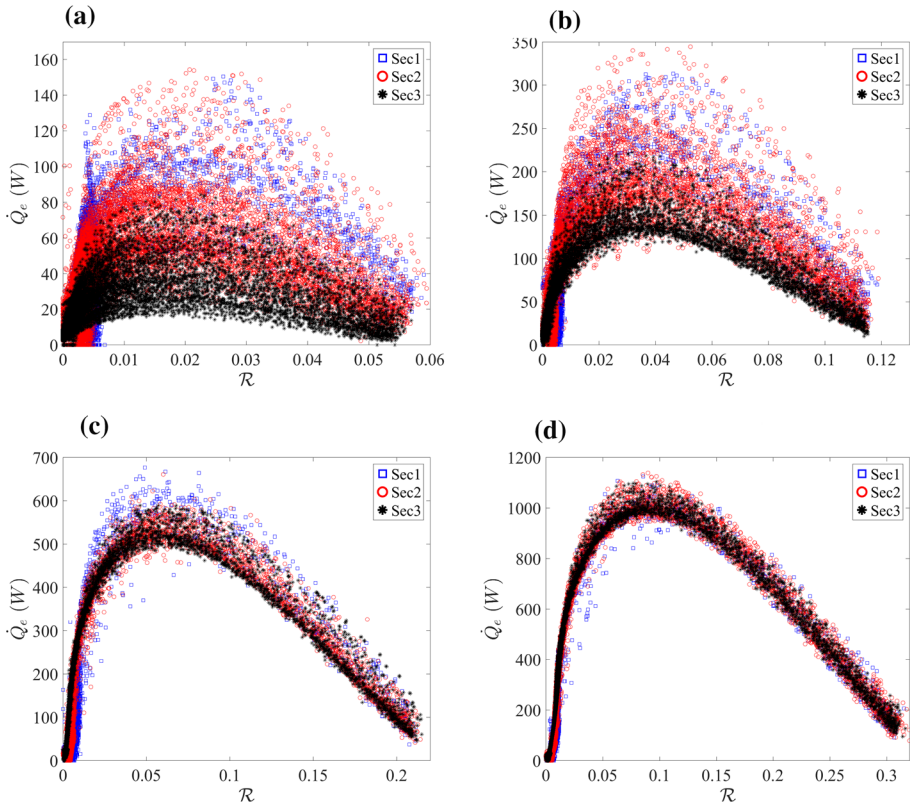


Fig. 15 Scatter plot of the heat release rate, \dot{Q}_e (W), versus TJI progress variable, \mathcal{R} , for **a** Case1, **b** Case2, **c** Case3, and **d** Case4 at different stream-wise sections represented by (blue square) Sec1, (red circle) Sec2, and (black asterisk) Sec3

general behavior in Fig. 15 is that the flame becomes much more intensive and the heat release rate roughly doubles on average with the increase in coflow equivalence ratio from 0.1 to 0.5 in Case1 to Case4. The maximum heat release happens at \mathcal{R} values corresponding to the flame front, i.e. $\mathcal{R} = 0.02, 0.04, 0.065, \text{ and } 0.1$. The areas with greater \mathcal{R} values correspond to the preheated zone of the premixed flame. The areas with smaller \mathcal{R} values represent either the hot product zone or the burned-mixed zone. The extent of scatter in the $\dot{Q}_e - \mathcal{R}$ plot also shows finite-chemistry effects and the level of local flame extinction. The very wide scatter in $\dot{Q}_e - \mathcal{R}$ data for the ultra-lean Case1 (with $\phi_{co} = 0.1$) indicates that the finite rate chemistry effects are indeed very important and the local heat loss is more than the heat release so that a stable and continuous flame can hardly be maintained. This becomes more clear when the results at different sections of the flow are compared. As stated before, the flame behavior in Case1 changes in the stream-wise direction from a complex thick flame in the nearfield region to a localized thin discontinuous flame in the developed region. In the nearfield region, as shown in Fig. 15a, the flame is stable and continuously provides sufficient amount of heat. This is represented by high \dot{Q}_e at low \mathcal{R} values and is also supported by H and \dot{Q}_e contours in Figs. 10a and 11a. Moving in the stream-wise direction to Sec2, lower \dot{Q}_e values at a given \mathcal{R} are observed. In Sec3, the extinction

is dominant and scatter in data is extensive in all flame regions. A somewhat similar but with less extensive scatter in the $\dot{Q}_e - \mathcal{R}$ data is observed for the Case2 (with $\phi_{co} = 0.2$) in Fig. 15b. For Case3 (with $\phi_{co} = 0.35$) and Case4 (with $\phi_{co} = 0.5$), the relatively small scatter in the $\dot{Q}_e - \mathcal{R}$ data in all sections or jet locations supports the existence of a strong, continuous, and stable premixed combustion.

The effects of turbulence and flow strain rate on the TJI-assisted combustion and flame stabilization are different than those in standard turbulent premixed flames. In the nearfield region, where the strain rate, $\dot{\epsilon}$, is high, the flow residence time is relatively small, which theoretically might lead to an incomplete reaction. However, hot eddies, mixing, and high turbulence levels in the nearfield region facilitate the heating of the coflow by the hot product jet. This overtakes the negative effects of the high strain rate and prevents local extinction in this region. Figure 16a, b present the scatters of the heat release rate (\dot{Q}_e) versus strain rate for Case1 and Case4. The data are separated for the three different sections in the stream-wise locations by different symbols and colors. Evidently, the strain rate varies in the same range in these two “extreme” cases, one with and one without extinguished flame zones. Therefore, unlike the standard turbulent premixed flames, a critical strain rate can not be defined for the simulated TJI-assisted combustion system. It is also observed in Fig. 16 that for the same strain rate the heat release rate is generally less significant further away from the inlet in Sec3 as compared to Sec1 and Sec2. This is mostly valid at higher strain rates. In Case4, most of the high heat release reaction happens in the low strain rate regions ($\dot{\epsilon} \leq 0.5 \times 10^4$) but in Case1 there are still significant high heat release values at moderate strain rate range ($0.5 \times 10^4 \leq \dot{\epsilon} \leq 2.0 \times 10^4$). In the developed region, Sec2 and Sec3 in Fig. 16a, the high strain rate values cause flame extinction while they also help the re-ignition by convection heat transfer from the main jet to the extinguished flame zones. This helps the flame to stabilize and eventually lowers the lean flammability limit.

The effects of TJI-assisted combustion on the turbulence and vice versa are further investigated by considering the jet thermal half width, the turbulence intensity, and the vorticity magnitude in Fig. 17. The solid thick lines in this figure show the results at maximum temperature rms, $\max(T_{rms})$, location and the dashed thin lines denote those at maximum turbulence intensity, $\max(I)$, location, where $I = \frac{(u'^2 + v'^2 + w'^2)^{\frac{1}{2}}}{U_{ref}}$. Figure 17a shows the

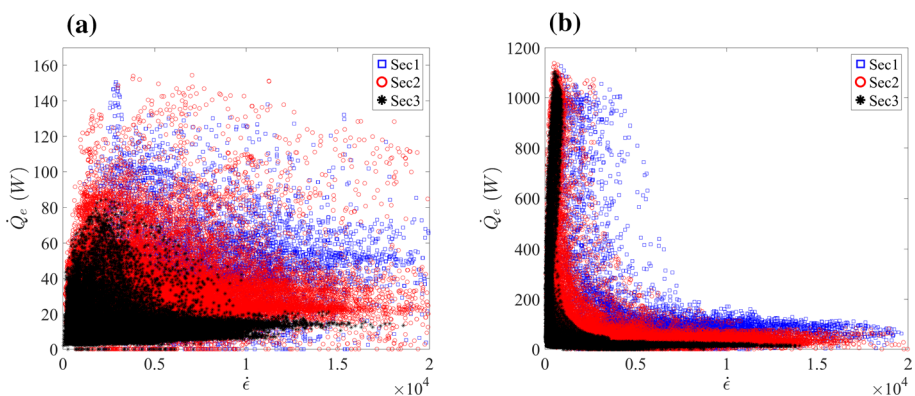


Fig. 16 Scatter plot of the heat release rate, \dot{Q}_e (W), versus strain rate, $\dot{\epsilon}$ (1/s), for **a** Case1 and **b** Case4 at different stream-wise sections represented by (blue square) Sec1, (red circle) Sec2, and (black asterisk) Sec3

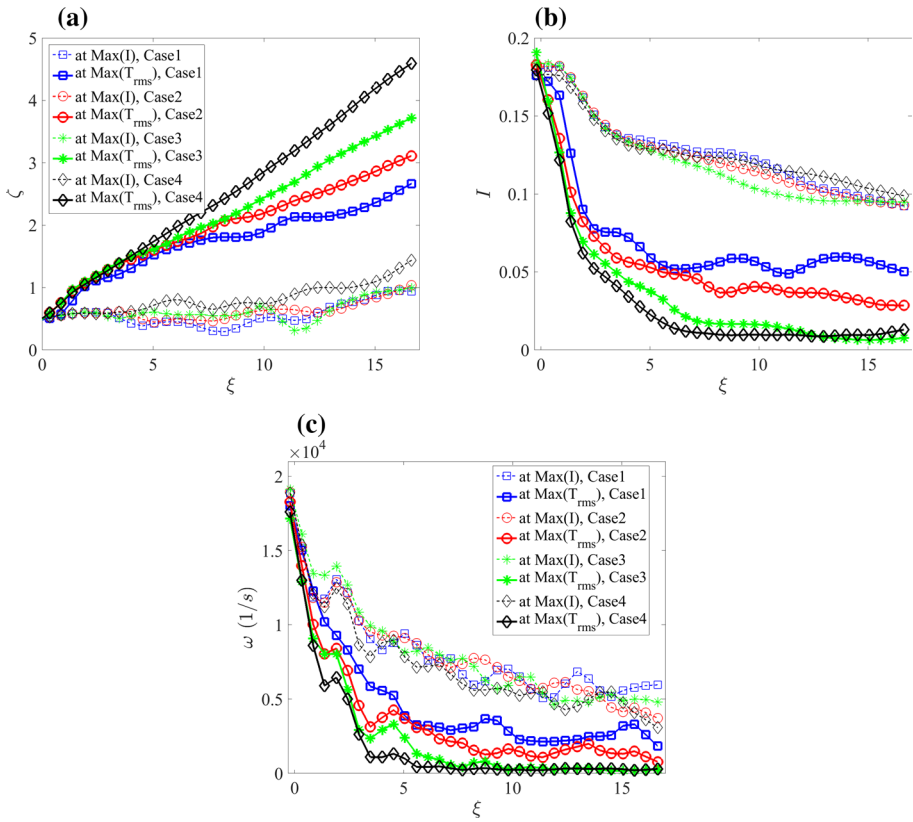


Fig. 17 **a** Cross-stream location of $\max(T_{rms})$ and $\max(I)$, **b** turbulence intensity, I , values at $\max(T_{rms})$ and $\max(I)$ locations, and **c** vorticity magnitude, ω , at $\max(T_{rms})$ and $\max(I)$ locations, versus stream-wise direction, ξ , for four cases represented by (blue square) Case1, (black diamond) Case2, (red circle) Case3, and (green asterisk) Case4. Thick solid and thin dashed lines correspond to $\max(T_{rms})$ and $\max(I)$ results, respectively

location of the maximum T_{rms} and I in the cross-stream direction versus the stream-wise direction. The $\max(T_{rms})$ can be used to identify the approximate location of the lean premixed flame and the jet thermal half width in the TJI-assisted combustion as it was shown in Fig. 6i. The location of the maximum turbulence intensity clearly differs from the location of flame or $\max(T_{rms})$. This confirms that as the premixed flame propagates into the coflow it gets separated from the core turbulence. It also suggests that the temperature field is not well correlated with the flow field and turbulence in the developed region. As expected, the jet span, estimated based on the $\max(I)$, increases by increasing the coflow equivalence ratio and the premixed flame moves further away from the incoming jet, leading to less interactions between them. The lowest jet growth corresponds to Case1. In this case, the premixed flame is very close to the turbulent jet and has the most significant damping effects on the turbulence and jet expansion in the cross-stream direction.

The turbulence intensity or I values at $\max(T_{rms})$ and $\max(I)$ locations are shown along the stream-wise direction in Fig. 17b. Close to the jet inlet, the I values at these locations are almost the same in all four cases. The small differences could be related to small variations in the coflow density. The lower I values at $\max(T_{rms})$ for Case3 and Case4 indicate

the significant separation of the premixed flame from the inner turbulent jet. The peak turbulent intensity is generally lower in these two cases because of combustion damping effects on turbulence. The I values at the $\max(I)$ locations similarly decrease in the stream-wise direction, however, they are about one order of magnitude higher than those at the flame location, which shows the nearly flame independent behavior of the hydrodynamics in these cases. The I values at any locations in the developed region are greater for the cases with higher equivalence ratios, Case4 and Case3, which again confirms the less interactions of the flame with turbulence. The I values at flame location or $\max(T_{rms})$ in Case1 and Case2 are considerably higher than those in Case3 and Case4 due to relatively weak premixed flame and an extensive overlap between jet turbulence and flame; the higher the coflow equivalence ratio, the lower the I at flame location. It is to be noted that the locations and values of $\max(T_{rms})$ and $\max(I)$ at shear layer in the nearfield region are similar in these four cases (Fig. 17a, b).

In Fig. 17c, the stream-wise variations of vorticity magnitude, $\omega = |\vec{\omega}|$, at $\max(T_{rms})$ and $\max(I)$ locations for Case1 to Case4 are compared. The ω levels in the nearfield region are relatively high because of the intense interactions between the incoming turbulent jet and premixed flame. At the end of the nearfield region, the flow is transitioning to the developed region, while the combustion starts to affect the flow. In the developed region, however, the flame–turbulence interactions are more important in Case1 and to some extent in Case2. As observed in Fig. 17c, the vorticity magnitudes at $\max(T_{rms})$ locations reach to very low values in the cases with a stable and strong combustion (Case3 and Case4); supporting the fact that the combustion has a strong dissipative effect on turbulence. Nevertheless, the simulated hot product jet is highly turbulent with significant fluctuations in flow variables at all length (and time) scales, even though the small-scale turbulent structures are depleted by the combustion. In the nearfield region and at $\max(I)$ locations, the vortex stretching and compressibility are the sources of the vorticity production. Further downstream in the developed region, the significant variations in density and pressure cause the Baroclinic torque, $\vec{\beta} = \frac{1}{\rho} \nabla \rho \times \nabla P$, to play a more important role in generating the vorticity. Close to the flame zone at $\max(T_{rms})$ locations, the Baroclinic torque and the vortex stretching are the main sources of generating vorticity. Nevertheless, close to the flame the vorticity field is negatively affected by the reaction because of heat release induced volumetric flow expansion and temperature dependency of viscosity. In the nearfield region, $\vec{\beta}$ is generated mainly due to density difference between the incoming hot jet and coflow and the density/pressure gradient generated in the inner jet core by the complex thick flames. In the developed region, however, the main reasons for the Baroclinic torque generation are the heat transport and lean premixed combustion in the outer edge of flow.

4.3 Incoming Jet Thermo-Chemical Effects

In this section, the effects of incoming jet thermo-chemical conditions on the TPJ–TJI are investigated by comparing the results for Case3, Case5, and Case6. In these cases the equivalence ratio of the initial jet mixture, and consequently the incoming jet composition and temperature, are different while the coflow conditions are the same. In Case3, the inflow jet composition is that of the combustion products of a stoichiometric mixture with no extra fuel or oxidizer with $T_j = 2556\text{K}$ (K). In Case5, the initial mixture equivalence ratio is chosen to be on the lean side with $\phi_j = 0.5$, thus the jet mainly consists of O_2 and H_2O with relatively lower (compared to Case3) temperature of $T_j = 2050$ (K). In Case6, a rich initial jet mixture is considered, therefore the incoming jet carries significant unburned

hot fuel along with the combustion products (mainly H_2O) with temperature of $T_j = 2350$ (K). This makes the flame a combination of premixed and diffusion type, very different than that in Case3 and Case5. The jet and the coflow hydrodynamics are considered to be the same in these three cases.

Figure 18a, b show the instantaneous OH mass fraction contours at time $t = 17\tau_0$ for Case5 and Case6, respectively. In the nearfield region, the intense and similar production of OH radical in Case5 and Case6 once again show the significance of chemical reaction and the strong flame–turbulence interactions. In Case5, the OH mass fraction in the incoming jet is relatively low (around $1.8e-3$), but the y_{OH} values are high in the developed region particularly in the burned-mixed and product jet zones. The high level of y_{OH} is mostly due to the nearfield combustion products which are transported downstream by the turbulent jet. This is consistent with the \dot{Q}_e results in Fig. 18e, which shows that the heat release in the developed region is small. In Case6, the jet OH mass fraction value is equal to $9.9e-4$ which is the lowest value among all three cases. However, the highest y_{OH}

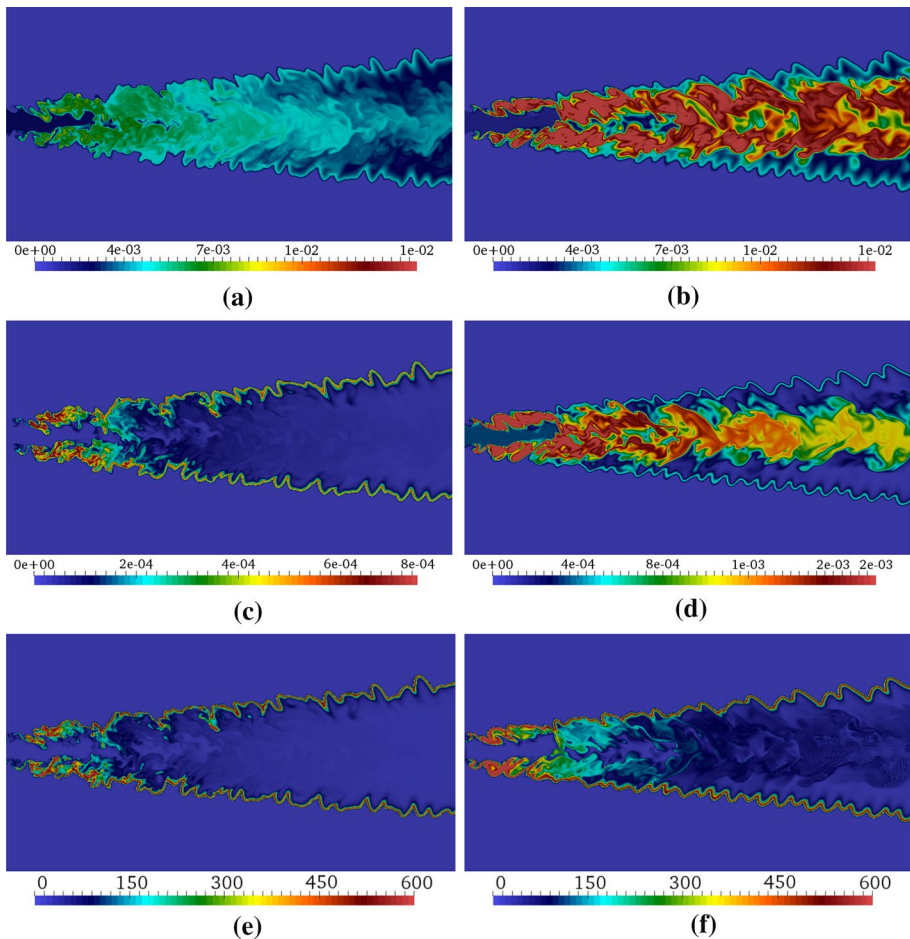


Fig. 18 Instantaneous contours of **a, b** OH mass fraction, y_{OH} , **c, d** H mass fraction, y_H , **e, f** heat release rate, \dot{Q}_e (W) at the mid span-wise plane ($z = 1.5D$) and $t = 17\tau_0$ for **a, c, and d** Case5; and **b, d, and f** Case6

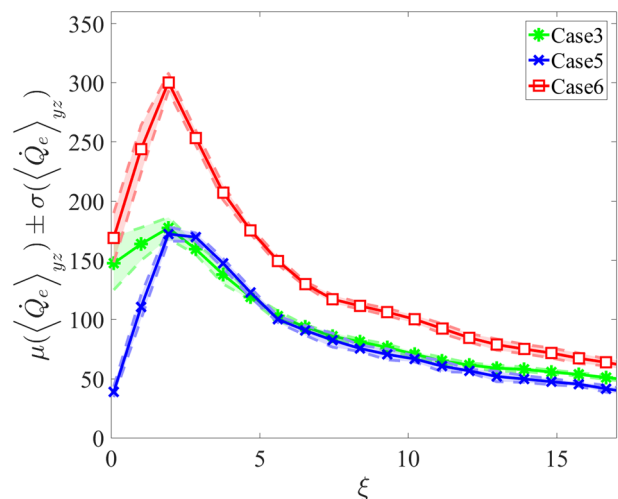
values are seen in the developed region for this case, which is mainly due to reaction of the unburned fuel inside the incoming jet with the hot residual oxygen of the lean coflow combustion. These results suggest that it is somewhat difficult to capture the premixed and non-premixed flames in the TPJ–TJI combustion by the OH radical.

Figure 18c, d present the H mass fraction contours for Case5 and Case6. The y_H levels in the incoming jets are very low ($1.3e-6$ and $3.3e-4$). Therefore, most of H radicals in the domain are produced by the premixed and non-premixed combustion. The nearfield results in Fig. 18c, d indeed show that significant H radicals are generated by the very complicated, thick, and distributed combustion in both cases, even though the H radical generation in the case with extra fuel is much more significant. In the developed region, the H radical distribution provides a view on the flame structure and its location. In Case5 (similar to Case1 to Case4), the maximum value of y_H is located at the lean premixed flame front, while y_H values are relatively very low in other zones. In Case6, the H radical concentration is significant not only at the premixed flame zones, but also inside the hot product jet zone, where strong diffusion flames exist (Fig. 18d). This behavior is consistent with the heat release contours shown in Fig. 18f.

Figure 18e, f present the instantaneous contours of heat release rate for Case5 and Case6 at $t = 17\tau_0$. The flame/turbulence structures in the nearfield and developed regions of Case5 are very similar to those shown before for Case3. However, due to lower incoming jet temperature, the amount of heat release in the nearfield region is slightly lower, which indicates less heat transfer and the initiation of combustion at lower temperatures. It was observed in Fig. 3c, e that the overall combustion zone temperature in Case5 is lower than that in Case3 due to less heat transfer from the incoming jet to its surroundings. However, since the combustion in the developed region is mainly controlled by the coflow conditions, almost the same amount of heat is generated by the premixed combustion in this region. This is also observed in Fig. 19, where the mean and the confidence bounds of \dot{Q}_e in the combustion zones are plotted at different stream-wise locations.

Despite the overall similarities of the thermal half width jet growth in Case6 with those in Case5 and Case3, the flame type and combustion behavior in this case are quite different.

Fig. 19 Mean and confidence intervals of $y-z$ plane averaged heat release rate, $\mu(\langle \dot{Q}_e \rangle_{yz}) \pm \sigma(\langle \dot{Q}_e \rangle_{yz})$, at $t = 17\tau_0$ versus stream-wise direction, ξ , for Case3 (green asterisk), Case5 (blue times), and Case6 (red right-pointing triangle)



In Case6, the flame–turbulence interactions in the nearfield region are more complex due to the existence of unburned hot fuel in the incoming jet and very significant diffusion flame in the jet zone. The wide and high level of \dot{Q}_e in the nearfield region indeed represents the extensive overlap of thick and distributed premixed flame with the diffusion flame. Moving in the stream-wise direction, a spatially continuous and distorted premixed flame is developed in Case6 which gradually propagates and gets separated from the jet. This is similar to what we observed for Case3 and Case5 and is represented by a moderate level of \dot{Q}_e at the edge of the flow. The heat release values in the inner jet are due to diffusion flames.

Figure 19 shows that the planar averaged heat release values in Case6 are considerably higher than those in other cases even though the coflow conditions are the same. This supports the existence of diffusion reaction of the extra fuel with the entrained lean coflow mixture into the incoming jet. Note that despite the effectiveness of diffusion combustion, some of the extra fuel in the incoming jet could still survive and exit the domain due to lack of oxygen or a long mixing time. The amount of unburned fuel can be controlled by the initial mixture and coflow equivalence ratios, ϕ_{ij} and ϕ_{co} , and the turbulence in the jet and even coflow. Lower (but still greater than one) values of ϕ_{ij} results in less unburned fuel in the incoming jet and lower ϕ_{co} leads to higher remainder oxidizer after the lean premixed combustion.

In Figs. 20a, b the scatter plot of \dot{Q}_e versus \mathcal{R} are shown for Case5 and Case6 at different sections of the flow. Similar to Case3, the maximum heat release occurs at $\mathcal{R} \approx 0.065$ in these two cases, which corresponds to the premixed flame front. The observations and explanations made before for Case3 are also valid for the premixed flames in Case5 and Case6. However, the non-premixed flame in Case6 can also be identified by $\dot{Q}_e - \mathcal{R}$ scatter plot in Fig. 20b. The non-premixed flame zone of the simulated TJI-assisted combustion system has a relatively high temperature and \mathcal{R} values in Case6 when compared to Case3. As it can be seen in Fig. 20b, the \mathcal{R} values associated with the non-premixed flame constantly decrease along the stream-wise direction, indicating stronger non-premixed combustion in the nearfield region. This was also shown in Fig. 8i where the temperature in the combustion zones is plotted versus \mathcal{R} for Case6. Larger \mathcal{R} values at high temperature zones represent the non-premixed combustion. A comparison between \dot{Q}_e scatter plots for Case5 (with extra oxygen) and Case6 (with extra fuel) indicates that by excluding the

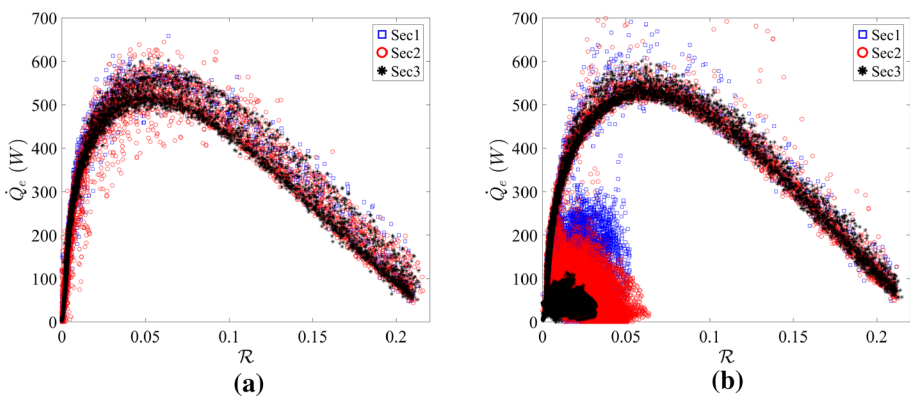


Fig. 20 Scatter plot of the heat release rate, \dot{Q}_e (W), versus TJI progress variable, \mathcal{R} , for **a** Case5 and **b** Case6 in different stream-wise sections, represented by (blue square) Sec1, (red circle) Sec2, and (black asterisk) Sec3

non-premixed flame, the results are similar in these two cases, with slightly more scatter in the lean burned jet Case5.

The results in Figs. 18, 19, and 20 indicate the existence of a combined premixed and non-premixed combustion when there is an extra fuel in the hot product jet stream. However, the premixed and non-premixed flames are somewhat separated in physical space due to propagation of premixed flame and confinement of the main jet. This can change if the premixed flame becomes weaker for much lower coflow equivalence ratio or ultra-lean conditions such as those considered in Case1. As discussed in Sect. 4.2 and shown in Figs. 9, 10, 11, 12, 13, 14, 15, 16, and 17, the highly unsteady and unstable premixed flame in this case experiences significant finite-rate chemistry effects and considerable local extinction and re-ignition. Here, we investigate the effects of extra fuel in the incoming jet and the developed diffusion flame on the ultra-lean TPJ–TJI set up by considering Case7 which has the same coflow conditions as Case1 and the same incoming jet as Case6.

Figure 21a, b show the instantaneous temperature and H mass fraction contours at time $t = 17\tau_0$ for Case7. In the nearfield region these contours are very similar to those in Figs. 3f and 18d, confirming the significance of the inflow conditions. However, the flame/flow structures in the developed region of Case7 are very different than those observed in the other cases. The premixed flame propagation in Case7 is less, therefore, the thermal half width of the jet is almost the same as that in Case1. However, the temperature and H radicals generation in the reacting zones are higher, showing the dominance of the diffusion flame in the developed region. Nevertheless, the premixed and diffusion flame structures are still captured by the H radical; the high and low y_H values represent the diffusion and premixed flames, respectively.

In Fig. 22a, the heat release (\dot{Q}_e) contours for Case7 are shown together with a magnified view of a section of the flow/flame field are shown. The magnified section which is located in the developed region, is the same spacial TPJ–TJI section considered for Case1 in Fig. 13. The highest values of \dot{Q}_e mainly occur in the nearfield region, hence, for a better visualization, a relatively low contour maximum value (200 W), representing the heat release values in the developed region, is considered. The premixed and diffusion flames are shown with dot and dashed lines, respectively. Since the coflow involves an ultra-lean fuel–air mixture, the premixed flame propagation in the cross-stream direction is weak. This leads to an extensive overlap between premixed and diffusion flames and smaller burned-mixed zone. The interactions of the weak premixed flame and high temperature diffusion flame develop a fairly stable premixed flame in the ultra-lean fuel–air mixture.

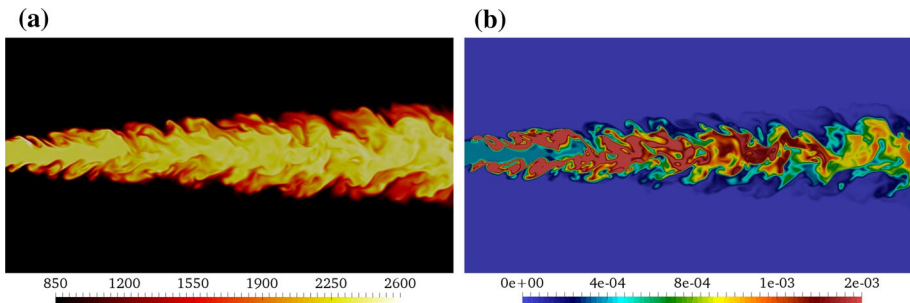


Fig. 21 Instantaneous contours of **a** temperature and **b** H mass fraction, y_H at the mid span-wise plane ($z = 1.5D$) and $t = 17\tau_0$ for Case7

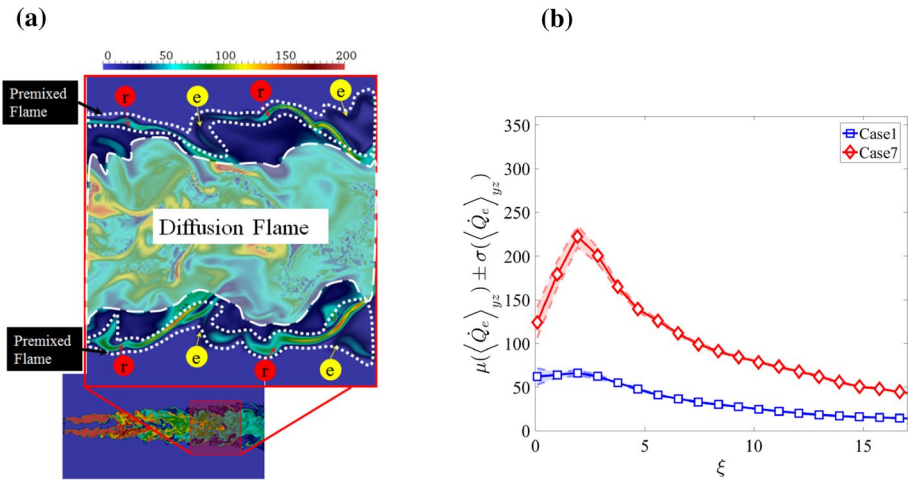


Fig. 22 **a** Simultaneous existence of diffusion and premixed flames along with localized extinction **e** and re-ignition **r** events at the premixed flame surrounding the diffusion flame in Case7 with the ultra-lean coflow and rich incoming jet, identified based on heat release and a magnified view of flow by a factor of 5:1. **b** Mean and confidence intervals of $y - z$ plane averaged heat release rate, $\mu(\langle \dot{Q}_e \rangle_{yz}) \pm \sigma(\langle \dot{Q}_e \rangle_{yz})$, at $t = 17\tau_0$ at different stream-wise locations, ξ , for Case1 (blue square) and Case7 (red circle)

Therefore, much less flame extinction and reignition events (as compared to Case1 in Fig. 13) occur. This can be further investigated by comparing the mean and confidence intervals of $y - z$ plane averaged heat release rate, $\mu(\langle \dot{Q}_e \rangle_{yz}) \pm \sigma(\langle \dot{Q}_e \rangle_{yz})$, at $t = 17\tau_0$ at different stream-wise locations, ξ , for Case7 and Case1 (Fig. 22b). Similar to previous cases the maximum values of $\mu(\langle \dot{Q}_e \rangle_{yz}) \pm \sigma(\langle \dot{Q}_e \rangle_{yz})$ occur in the nearfield region for the reasons explained before. Further downstream, the higher values of \dot{Q}_e confirm less localized extinction in the premixed flame of Case7 when compared to that in Case1. The premixed flame in the former is more like a continuous flame with less discontinuities due to localized extinction even at very high strain rate locations, showing the uniqueness of the simulated ultra-lean hybrid premixed-diffusion flame.

5 Summary and Conclusions

Direct numerical simulations of a hot product turbulent planar jet (TPJ) injected into a lean premixed hydrogen–air coflow are performed with detailed chemical kinetics to study turbulent jet ignition (TJI)-assisted combustion in a fundamental three-dimensional configuration. The TPJ–TJI system is spatially divided into nearfield and developed regions. In the nearfield region, the hot incoming jet rapidly auto ignites the lean hydrogen–air mixture at the developing jet shear layer, creating a complex flame structure and providing significant energy for a sustainable ultra-lean combustion. In the developed region, three main combustion zones are identified:

- (1) remnant of the hot product jet zone,
- (2) burned-mixed zone, and
- (3) premixed flame zone.

The jet “thermal width” is shown to be dependent more on the coflow thermo-chemical conditions than the incoming jet composition. However, the flame structure is still highly affected by the incoming turbulent jet temperature and composition. In one case the reaction of the unburned hot fuel available in the jet with the remaining oxygen from the lean premixed flame creates a complex combination of premixed and non-premixed flames. To examine the flame structure, a new TJI progress variable is defined based on the local temperature and mixture composition. The interactions between the premixed flame zone and the hot turbulent inner jet are shown to be much more intense in ultra-lean coflow mixtures, generating extensive localized flame extinction and re-ignition events. Scatter plots of the local flow temperature, species mass fraction, and strain rate versus TJI progress variable show significant finite rate chemistry and damping effects of combustion on the turbulence field. The lean flammability limit is shown to be considerably lowered by TJI despite the existence of localized flame extinction. In the TJI-assisted combustion, the premixed flame gets separated more from the inner turbulent jet as it propagates into the lean coflow mixtures with higher equivalence ratios. This affects the inner jet flow and turbulence. Turbulence intensity and vorticity values are shown to be much smaller at the flame location in premixed flames propagating faster into coflows because of higher equivalence ratios, while they always maximize at the edge of the inner turbulent jet or the shear layers. Our analysis also indicates that the temperature and velocity fields are not well correlated; an important issue in the modeling of TJI-assisted combustion systems. In the case of rich burned incoming product jet, the mixed diffusion-premixed flames are developed in the TJI-assisted combustion which show very complex hybrid flame structures.

Acknowledgements This study was conducted with the support of NSF and DOE under Grant Number CBET-1258581. The authors would also like to thank the Texas Advanced Computing Center at the University of Texas-Austin and the Institute for Cyber-Enabled Research at Michigan State University for providing high performance computational resources.

Funding This study was funded by NSF and DOE under Grant Number CBET-1258581.

Compliance with Ethical Standards

Conflict of interest The authors declare that they have no conflict of interest.

References

- Afshari, A., Jaber, F., Shih, T.: Large-eddy simulations of turbulent flows in an axisymmetric dump combustor. *AIAA J.* **46**(7), 1576 (2008)
- Arndt, C., Schiel, R., Gounder, J., Meier, W., Aigner, M.: Flame stabilization and auto-ignition of pulsed methane jets in a hot coflow: influence of temperature. *Proc. Combust. Inst.* **34**(1), 1483–1490 (2013)
- Banaeizadeh, A., Li, Z., Jaber, F.: Compressible scalar filtered mass density function model for high-speed turbulent flows. *AIAA J.* **49**(10), 2130 (2011)
- Banaeizadeh, A., Afshari, A., Schock, H., Jaber, F.: Large-eddy simulations of turbulent flows in internal combustion engines. *Int. J. Heat Mass Transf.* **60**, 781–796 (2013)
- Beerer, D., McDonnell, V., Therkelsen, P., Cheng, R.K.: Flashback and turbulent flame speed measurements in hydrogen/methane flames stabilized by a low-swirl injector at elevated pressures and temperature. *J. Eng. Gas Turbines Power* **136**, 20242–20254 (2014)
- Bezgin, L., Kopchenov, V., Sharipov, A., Titova, N., Starik, A.: Evaluation of prediction ability of detailed reaction mechanisms in the combustion performance in hydrogen/air supersonic flows. *Combust. Sci. Technol.* **185**(1), 62–94 (2013)

- Bisetti, F., Abdelgadir, A., Steinmetz, S., Attili, A., Roberts, W.: Self-similar scaling of pressurised sooting methane/air coflow flames at constant Reynolds and Grashof numbers. *Combust. Flame* **196**, 300–313 (2018)
- Boivin, P., Dauptain, A., Jiménez, C., Cuenot, B.: Simulation of a supersonic hydrogen/air autoignition-stabilized flame using reduced chemistry. *Combust. Flame* **159**(4), 1779–1790 (2012)
- Clavin, P.: Dynamic behavior of premixed flame fronts in laminar and turbulent flows. *Progress Energy Combust. Sci.* **11**(1), 1–59 (1985)
- Denker, D., Attili, A., Luca, S., Bisetti, F., Gauning, M., Pitsch, H.: Dissipation element analysis of turbulent premixed jet flames. *Combust. Sci. Technol.* **191**(9), 1677–1692 (2019)
- Djebaili, N., Lisbet, R., Dupre, G., Patillard, C.: Ignition of a combustible mixture by a hot unsteady gas jet. *Combust. Sci. Technol.* **104**, 273–285 (1995)
- Dorofeev, S., Bezmelnitsin, A., Sidorov, V., Yankin, J., Matsukov, I.: Turbulent jet initiation of detonation in hydrogen–air mixtures. *Shock Waves* **6**(2), 73–78 (1996)
- Gordeyev, S., Thomas, E.: Coherent structure in the turbulent planar jet. Part 1. Extraction of proper orthogonal decomposition eigenmodes and their self-similarity. *J. Fluid Mech.* **414**, 145–194 (2000)
- Gunnar, H.: Hot-wire measurements in a plane turbulent jet. *J. Appl. Mech.* **32**(4), 721–734 (1965)
- Hinze, J.: *Turbulence*. McGraw-Hill, New York (1975)
- Iglesias, I., Vera, M., Sanchez, A.L., Linan, A.: Numerical analyses of deflagration initiation by a hot jet. *Combust. Theory Model.* **16**(6994), 994–1010 (2012)
- Jaberi, F., James, S.: A dynamic similarity model for large eddy simulation of turbulent combustion. *Phys. Fluids* **10**(7), 1775–1777 (1998)
- Jaberi, F., Miller, R., Mashayek, F., Givi, P.: Differential diffusion in binary scalar mixing and reaction. *Combust. Flame* **109**(4), 561–577 (1997)
- Jaberi, F., Colucci, P., Colucci, S., Givi, P., Pope, S.: Filtered mass density function for large-eddy simulation of turbulent reacting flows. *J. Fluid Mech.* **401**, 85–121 (1999)
- James, S., Jaberi, F.: Large scale simulations of two-dimensional nonpremixed methane jet flames. *Combust. Flame* **123**(4), 465–487 (2000)
- Jin, T., Luo, K., Lu, S., Fan, J.: DNS investigation on flame structure and scalar dissipation of a supersonic lifted hydrogen jet flame in heated coflow. *Int. J. Hydrogen Energy* **38**(23), 9886–9896 (2013)
- Ju, Y., Niioka, T.: Reduced kinetic mechanism of ignition for nonpremixed hydrogen/air in a supersonic mixing layer. *Combust. Flame* **99**, 240–246 (1994)
- Kee, R., Rupley, F., Miller, J.: *Chemkin-II: a Fortran chemical kinetics package for the analysis of gas-phase chemical kinetics* (1989)
- Kennedy, C., Carpenter, M., Lewis, R.: Low-storage, explicit Runge–Kutta schemes for the compressible Navier–Stokes equations. *Appl. Numer. Math.* **35**(3), 177–219 (2000)
- Kerstein, A.: Linear-eddy modeling of turbulent transport. Part 4. Structure of diffusion flames. *Combust. Sci. Technol.* **81**(1–3), 75–96 (1992)
- Klimenko, A., Bilger, R.: Conditional moment closure for turbulent combustion. *Progress Energy Combust. Sci.* **25**(6), 595–687 (1999)
- Kotsovinos, N.: A note on the spreading rate and virtual origin of a plane turbulent jet. *J. Fluid Mech.* **77**, 305–311 (1976)
- Lele, S.: Compact finite difference schemes with spectral-like resolution. *J. Comput. Phys.* **103**(1), 16–42 (1992)
- Li, Z., Banaeizadeh, A., Rezaeiravesh, S., Jaberi, F.: Advanced modeling of high speed turbulent reacting flows. In: 50th AIAA Aerospace Sciences Meeting (2012)
- Lin, Y., Jansohn, P., Boulouchos, K.: Turbulent flame speed for hydrogen-rich fuel gases at gas turbine relevant conditions. *Int. J. Hydrogen Energy* **39**(35), 20242–20254 (2014)
- Lu, S., Fan, J., Luo, K.: High-fidelity resolution of the characteristic structures of a supersonic hydrogen jet flame with heated co-flow air. *Int. J. Hydrogen Energy* **37**(4), 3528–3539 (2012)
- Luca, S., Attili, A., Schiavo, E., Creta, F., Bisetti, F.: On the statistics of flame stretch in turbulent premixed jet flames in the thin reaction zone regime at varying Reynolds number. *Proc. Combust. Inst.* **37**(2), 2451–2459 (2019)
- Madnia, C., Jaberi, F., Givi, P.: Large eddy simulation of heat and mass transport in turbulent flows. In: Sparrow, E.M., Minkowycz, W.J., Murthy, J.Y. (eds.) *Handbook of Numerical Heat Transfer*, pp. 167–189. Wiley, Hoboken (2000)
- Mittal, G., Raju, M., Sung, S.: CFD modeling of two-stage ignition in a rapid compression machine: assessment of zero-dimensional approach. *Combust. Flame* **157**(7), 1316–1324 (2010)
- Najm, H., Paul, P., Mueller, C., Wyckoff, P.: On the adequacy of certain experimental observables as measurements of flame burning rate. *Combust. Flame* **113**(3), 312–332 (1998)

- Nikolaou, Z., Swaminathan, N.: Heat release rate markers for premixed combustion. *Combust. Flame* **161**(12), 3073–3084 (2014)
- Paul, P., Najm, H.: Planar laser-induced fluorescence imaging of flame heat release rate. *Symp. Int. Combust.* **27**(1), 43–50 (1998)
- Peters, N.: Laminar diffusion flamelet models in non-premixed turbulent combustion. *Progress Energy Combust. Sci.* **10**(3), 319–339 (1984)
- Peters, N.: Laminar flamelet concepts in turbulent combustion. *Symp. Int. Combust.* **21**(1), 1231–1250 (1988)
- Phillips, H.: Ignition in a transient turbulent jet of hot inert gas. *Combust. Flame* **19**(2), 187–195 (1972)
- Pierce, C., Moin, P.: Progress-variable approach for large-eddy simulation of non-premixed turbulent combustion. *J. Fluid Mech.* **504**, 73–97 (2004)
- Poinsot, T., Lelef, S.: Boundary conditions for direct simulations of compressible viscous flows. *J. Comput. Phys.* **101**(1), 104–129 (1992)
- Pope, S.: Calculation of a plane turbulent jet. *AIAA J.* **22**(7), 896–904 (1983)
- Pope, S.: Pdf methods for turbulent reactive flows. *Progress Energy Combust. Sci.* **11**(2), 119–192 (1985)
- Pope, S.: Turbulent premixed flames. *Annu. Rev. Fluid Mech.* **19**, 237–270 (1987)
- Pope, S.: *Turbulent Flows*. Cambridge University Press, New York (2000)
- Rehm, J.: The relationship between vorticity/strain and reaction zone structure in turbulent non-premixed jet flames. *Symp. Int. Combust.* **27**(1), 1113–1120 (1998)
- Rutland, C., Trouvé, A.: Direct simulations of premixed turbulent flames with nonunity Lewis numbers. *Combust. Flame* **94**(1–2), 41–57 (1993)
- Sadanandan, R., Markus, R., Schießl, R., Maas, U., Olofsson, J., Seyfried, H., Richter, M., Aldén, M.: Detailed investigation of ignition by hot gas jets. *Proc. Combust. Inst.* **31**(1), 719–726 (2007)
- Seitzman, J., Lieuwen, T.: Turbulent flame propagation characteristics of high hydrogen content fuels
- Stahl, G., Warnatz, J.: Numerical investigation of time-dependent properties and extinction of strained methane and propane–air flamelets. *Combust. Flame* **85**, 285–299 (1991)
- Steinberger, C., Vidoni, T., Givi, P.: The compositional structure and the effects of exothermicity in a non-premixed planar jet flame. *Combust. Flame* **94**(3), 217–232 (1993)
- Vagelopoulos, C., Egolfopoulos, F., Law, C.: Further considerations on the determination of laminar flame speeds with the counterflow twin-flame technique. *Symp. Int. Combust.* **25**(1), 1341–1347 (1994)
- Validi, A.: High fidelity numerical simulations of turbulent jet ignition and combustion. Ph.D. Thesis, Michigan State University (2016)
- Validi, A., Jaber, F.: Numerical study of turbulent jet ignition in a lean premixed configuration. *Flow Turbul. Combust.* **10**(1), 197–224 (2018)
- Validi, A., Schock, H., Jaber, F.: Turbulent jet ignition assisted combustion in a rapid compression machine. *Combust. Flame* **186**, 65–82 (2018)
- Wang, H., Luo, K., Lu, S., Fan, J.: Direct numerical simulation and analysis of a hydrogen/air swirling premixed flame in a micro combustor. *Int. J. Hydrogen Energy* **36**(21), 13838–13849 (2011)
- Wang, J., Yu, S., Zhang, M., Jin, W., Huang, Z., Chen, V., Kobayashi, H.: Burning velocity and statistical flame front structure of turbulent premixed flames at high pressure up to 1.0 MPa. *Exp. Therm. Fluid Sci.* **68**, 196–204 (2015)
- Yaldizli, M., Mehravaran, K., Mohammad, H., Jaber, F.: The structure of partially premixed methane flames in high-intensity turbulent flows. *Combust. Flame* **154**(4), 692–714 (2008)
- Zabetakis, M.: Flammability characteristics of combustible gases and vapors. U.S. Bureau of Mines. Bulletin 627 (1965)